



Norwegian University of
Science and Technology

Development of Hydrophobic Surfaces for Anti-Icing Applications

Hanna Sandvoll Vassmyr

Nanotechnology

Submission date: June 2016

Supervisor: Hilde Lea Lein, IMTE

Co-supervisor: Sidsel Meli Hanetho, SINTEF Materials and Chemistry
Christian Simon, SINTEF Materials and Chemistry
Per Stenstad, SINTEF Materials and Chemistry

Norwegian University of Science and Technology
Department of Materials Science and Engineering

Abstract

Icing is a problem for several actors in the industrial sector, and current methods for removal of ice have several difficulties. They are time consuming, energy intensive and may be environmentally harmful. A better solution to the icing problem is the introduction of an anti-icing surface which hinders ice formation and reduces ice adhesion if formed. Such surfaces have received a great deal of attention the last years, and one of the most investigated candidates is superhydrophobic surfaces. Such surfaces offer several advantages as they repel water, reduce the probability of ice formation due to low contact area, and can reduce ice adhesion. However, their durability and performance in icing conditions have been questioned.

In this work superhydrophobic surfaces, exhibiting contact angles above 150° and roll-off angles lower than 10° , on steel have been produced by a simple and scalable method. The substrates have been sandblasted with both fine and coarse sand and SiO_2 -nanoparticles have been deposited, yielding a hierarchical surface structure. The surface chemistry has been altered by the addition of a hydrophobic coating layer based on the precursor 1H,1H,2H,2H-perfluorooctyltriethoxysilane. The method for depositing both nanoparticles and the hydrophobic top layer has been optimized by a systematic investigation of several coating techniques, including dip coating, spray coating, spin coating and vapor deposition. The surface with the best superhydrophobic properties was achieved when spray coating of nanoparticles was done on a steel surface sandblasted with fine sand, and the top layer was deposited by dip coating. The surface achieved a contact angle of $158 \pm 2^\circ$ with distilled water, a roll-off angle of $8 \pm 2^\circ$ and contact angle hysteresis of $19 \pm 3^\circ$.

Icing characteristics of the surfaces produced have been tested in an environmental chamber, where the barrier against ice formation, the delay of ice formation at -10°C and the cyclic icing/de-icing character have been investigated. The sample showing the best hydrophobic characteristic also showed the highest barrier against ice formation with a freezing temperature of -14.8°C . However, other samples showed longer freezing delays (>1 hour) and in general no direct correlation between hydrophobic properties and anti-icing properties was found. In addition, the hydrophobic character of the surfaces was found to depend largely on the humidity and temperature, and no samples showed contact angles above 150° when cooled down to 5°C .

Sammendrag

Isdannelse er et stort problem i flere industrier, og dagens metoder for å fjerne is er tidkrevende, energiintensive og lite miljøvennlige. En bedre løsning på isproblemet er anti-isende overflater, overflater som hindrer is fra å dannes samt minker heften mellom is og overflate. Slike overflater har blitt mye studert de siste årene, og spesielt har det vært et stort fokus på superhydrofobe overflater. Superhydrofobe overflater frastøter vann, minker kontaktarealet mellom dråpe og overflate som reduserer sannsynligheten for at is dannes, og minker heften mellom is og overflate. Samtidig er holdbarheten gjennom flere isesykluser og egenskaper under iseforhold ikke optimale.

I denne masteroppgaven har superhydrofobiske overflater, overflater som har kontaktvinkler over 150° og rullevinkler under 10° , blitt laget på stål 316 ved en enkel og skalerbar metode. Substratene har blitt sandblåst med fin og grov sand, og SiO_2 -nanopartikler har blitt deponert. Resultatet er en hierarkisk overflatestruktur. Kjemien til overflaten har blitt endret ved å legge på et hydrofobisk lag basert på 1H,1H,2H,2H-perfluoroktyltrioksylsilan. I oppgaven har metoden for deponering av nanopartikler og det hydrofobiske laget blitt optimalisert ved systematisk testing av flere teknikker. Disse inkluderer dypping, spraying, spinning og gassfasedeponering. En kombinasjon av å spraye på nanopartikler og dyppe substratet i den hydrofobe løsningen ga overflaten med de beste egenskapene. Den viste en kontaktvinkel med destillert vann på $158 \pm 2^\circ$, en rullevinkel på $8 \pm 2^\circ$ og en kontaktvinkelhysterese på $19 \pm 3^\circ$.

Isegenskapene til overflatene har blitt testet i et miljøkammer. Barrieren for å danne is på overflaten, hvor lang tid det tar før det fryser ved -10°C , samt sykliske egenskaper ved frysing og smelting har blitt testet. Prøven som hadde de beste hydrofobiske egenskapene, hadde også den høyeste barrieren for isdannelsen. På denne prøven frøs vandråpen først ved $-14,8^\circ\text{C}$. Ved -10°C var det andre prøver som hadde de lengste forsinkelsene av isdannelse, og på enkelte var dråpen flytende selv etter en time. Ingen generell korrelasjon mellom hydrofobisitet og isegenskaper ble funnet. I tillegg avslørte testene at de hydrofobe egenskapene var veldig avhengig av temperaturoppsett og luftfuktighet. Ved 5°C viste ingen av overflatene kontaktvinkler over 150° .

Preface

This master's thesis is the result of the work carried out during the spring of 2016, the last semester of the 5-year Master's degree program in Nanotechnology at the Norwegian University of Science and Technology (NTNU). The work was performed at the Inorganic Materials and Ceramics Research group, at the Department of Materials Science and Engineering.

Associate professor Hilde Lea Lein has been the main supervisor. The work has also been supported by SINTEF Materials and Chemistry, with Sidsel Meli Hanetho, Christian Simon, and Per Stenstad as co-supervisors. The research done has been a continuation of the work done by Raymond Luneng [1] and Ole-Bjørn Ellingsen Moe [2] the spring of 2015, as well as the project work done by the author the fall of 2015 [3]. Another master student, Vegard Hornnes, has also been working on the same project with the focus on a different substrate, aluminum. All of the experimental work in this thesis was carried out by the author.

Trondheim, 15.06.2016

Hanna Sandvoll Vassmyr

Acknowledgements

The work performed this semester has been challenging, frustrating and rewarding. The subject of anti-icing surfaces has proven to be very interesting, and the potential of the field immense.

The work could not have been performed without the help and guidance of several people. First of all, I would like to thank my main supervisor, Associate professor Hilde Lea Lein, for your valuable insights, positive feedback, and openness to my suggestions. The encouragement and valuable help from my co-supervisor, Sidsel Meli Hanetho, has been greatly appreciated. Together with Hilde you have made our weekly meetings very motivating. Thank you, Christian Simon and Per Stenstad, for your interest in the field and valuable feedback. Ole-Bjørn Ellingsen, Raymond Luneng and Vegard Hornnes also deserve a thank you for answering my questions and helping me get started.

I would also like to thank all the people giving me training on instruments, and helping me with lab equipment. The staff of the Department of Materials Science and Technology has proven to be most helpful.

Lastly, I would like to thank my classmates. The good atmosphere, helpful spirit of you all and our non-academic lunch discussions have been greatly appreciated. A special thanks to Henrik Riis for proof-reading my entire thesis and improving my writing.

Contents

Abstract	i
Sammendrag	iii
Preface	v
Acknowledgements	vii
List of Figures	xii
List of Tables	xiii
List of Abbreviations	xv
1 Introduction	1
1.1 Motivation	1
1.2 Aim of the Work	3
2 Theory	5
2.1 Superhydrophobicity	5
2.2 Anti-Icing Surfaces	9
2.3 Sol-Gel Synthesis	15
2.4 Deposition Techniques	19
3 Experimental	25
3.1 Substrate Treatment	25
3.2 Synthesis of NPs	27
3.3 Coating Preparation	28

3.4	Deposition Techniques	30
3.5	Characterization	37
4	Results	43
4.1	Microroughness	43
4.2	Coating Characterization	44
4.3	Nanoroughness	47
4.4	Wetting and Adhesion	51
4.5	Icing Characteristics	60
5	Discussion	69
5.1	Surface Structure	69
5.2	CA Measurements	72
5.3	Icing Experiments	77
6	Conclusion	83
7	Further work	85
	Bibliography	93
	Appendices	95
A		95
A.1	Synthesis of Nanoparticles	95
A.2	Synthesis of β -silane	95
A.3	Surface vs Chamber Temperature	96

List of Figures

1.1	Structures that are exposed to ice accumulation.	2
2.1	A droplet on a flat surface.	6
2.2	A droplet on a tilted surface.	6
2.3	Cassie-Baxter and Wenzel wetting states.	8
2.4	Illustrations of a) the lotus and b) the petal effect.	9
2.5	Scheme showing the effect of pH on the gel structure.	17
2.6	Mechanism for particle growth.	18
2.7	Schematic of the steady-state dip coating process.	20
2.8	Schematic of spray coating equipment.	21
2.9	Schematic diagram of the stages of the spin coating process.	22
2.10	Schematic of how bonding can occur.	22
3.1	Flow chart of the experimental procedure.	26
3.2	Schematic of tetraethyl orthosilicate.	27
3.3	Schematic of 1H,1H,2H,2H-perfluorooctyltriethoxysilane.	28
3.4	Image of the set up used for sol-gel synthesis.	29
3.5	Image of dip coating process.	30
3.6	The Exacta-coat automatic spray coater.	31
3.7	Equipment used for vapor deposition.	35
3.8	The DSA100 from Krüss used for contact angle measurements.	39
3.9	Droplets on flat and tilted surfaces.	40
3.10	Front view of TC40 environmental chamber.	41
3.11	Pictures showing the freezing process.	42
4.1	Comparison of profilometer scans of across a fine and coarse structure.	45
4.2	SEM image of F-SC2- β -DC used for determining particle size.	46

4.3	SEM image of a fine steel substrate dip coated with NPs.	47
4.4	Cross section of a dip coated coarse sample, showing an area covered by several layers of NPs.	48
4.5	SEM images of spray coated surfaces.	49
4.6	SEM image of spray coated surface.	50
4.7	SEM image of the surface obtained by 500 rpm SPC of NP-sol.	51
4.8	Surface structure obtained by SPC of nanoparticle.	52
4.9	Average contact and roll-off angles achieved with different coating methods for the β -silane.	54
4.10	SEM images taken in a) SE mode and b) BSE mode on the same area on sample F-SC3- β -5S-DC.	55
4.11	SEM images of surface structure obtained by one-step SC.	57
4.12	CA development as a function of temperature on sample F-SC3- β -DC.	59
4.13	Development of CA as a the temperature was decreased.	59
4.14	Mechanism of freezing on sample F-SC- β -5S-DC.	62
4.15	CA development during cooling in icing/de-icing cycles.	63
4.16	Wetting hysteresis on samples C1-SC3- β -5S-DC and F-Combo4.	65
4.17	CA development of 8 μ L droplet over time at a constant temperature of 20°C.	65
4.18	Mechanism of freezing on sample F-SC3- β -DC, first experiment.	67
4.19	Mechanism of freezing on sample F-Combo4	68
5.1	Aggregate of particles found on an SC sample.	71
5.2	Illustration of surface structures obtained by deposition of different amounts of NPs.	72
5.3	Importance of using the right baseline and fitting mode when measuring CA and CAH.	76
5.4	Change of wetting state under supercooling.	78
A.1	Recorded temperature as a function of the set temperature during cooling.	96

List of Tables

2.1	Advantages and disadvantages of strategies for making anti-icing coatings.	10
3.1	Chemicals used for synthesizing particles and their function. . . .	28
3.2	Chemicals used for synthesis of the β -silane sol and their function.	29
3.3	Parameters used for NP-sol deposition by SC.	32
3.4	Parameters used for β -40S-sol deposition by SC.	32
3.5	Parameters used for one step NP and β -40S-sol SC.	33
3.6	Parameters used for SPC of NP-sol.	33
3.7	Parameters used for VD of β -silane.	34
3.8	Overview of samples made in this work.	36
3.9	Program used for measuring viscosity of synthesized sols.	38
4.1	Surface roughness obtained by sandblasting with two different types of sand.	44
4.2	Viscosity and calculated densities of produced sols.	46
4.3	CAs, ROAs and CAHs achieved in this work.	53
4.4	CA as a function of temperature and humidity on F-SC3- β -DC.	58
4.5	Temperature required for formation of ice on the different samples.	61
4.6	Temperature required for ice formation as a function of cycles and CAs achieved before and after freezing.	64
4.7	Delay of ice formation at -10°C	66
A.1	Amount and properties of chemicals in NP synthesis.	95
A.2	Properties of chemicals used in sol synthesis.	96

List of Abbreviations

CA	Contact Angle
CA_{adv}	Advancing Contact Angle
CA_{rec}	Receding Contact Angle
CAH	Contact Angle Hysteresis
ROA	Roll-off Angle
NP	Nanoparticle
<i>β</i>-silane	1H,1H,2H,2H-perfluorooctyltriethoxysilane
SB	Sandblasted
DC	Dip Coating
SC	Spray Coating
SPC	Spin Coating
VD	Vapor Deposition
F	Fine
C	Coarse
SEM	Scanning Electron Microscopy
SE	Secondary Electron
BSE	Back-Scattered Electron

Chapter 1

Introduction

In the following chapter some motivation and background for, as well as the aim of, this thesis will be given.

1.1 Motivation

Formation and accumulation of ice is a problem for many structures and industries, especially in the cold areas of the world. In the airplane industry icing causes delays, increased wind resistance, and in the worst cases fatal accidents [4]. Ice accumulation on wind turbines reduces the efficiency and the ice can be shed from the turbine, potentially harming humans and structures around [5]. Power lines can potentially break if too much ice is accumulated, leaving areas without power and causing expensive reparations [6]. Ships move through arctic areas, and as the search for oil moves further north so does more supply vessels and oil platforms, making them more prone to ice accumulation [7]. Figure 1.1 shows examples of exposed structures.

Current solutions for combatting icing problems include de-icing fluid, active heating, spraying with warm water and mechanical removal [10,11]. Such processes may be energy intensive, ineffective, environmentally unfavorable, expensive and time consuming [6]. Another, and possibly better, approach is to make surfaces that can passively prevent ice from forming and ease ice removal. Such

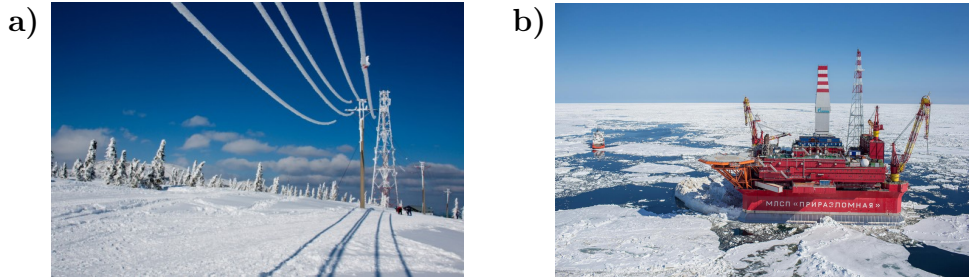


Figure 1.1: Structures that are exposed to ice accumulation. a) Powerline from [8] and b) oil platform from [9].

surfaces are called anti-icing surfaces, and have received attention in research communities lately. There is a wide discussion on which surfaces that have the best anti-icing abilities [12–16]. A recent Nature review, published in January 2016, sums up the possible solutions and much of the work done in the field [6]. The possible solutions include rough surfaces, slippery liquid-infused porous surfaces, and smooth bulk coatings. So far there is no single surface that has shown all the wanted icephobic properties, and there is still discussion around which solution is the best. Icephobicity includes shedding of incoming droplets, hindrance of ice formation from condensed water, suppressing ice nucleation and reducing the adhesion between the ice and the surface. The environmental conditions of the application also affect which solution works best.

For dry surfaces, the introduction of a micro- and nanostructure, have improved the surfaces humidity tolerance. Such surfaces, which also have a water-repellent chemistry, can be superhydrophobic. This involves the contact angle with water exceeding 150° , and a low angle of tilt required for the droplet to roll off the surface. A superhydrophobic surface has a small contact area with water droplets, which can reduce the probability of ice forming due to reduced heat transfer from the surface to the droplet and reduced probability for heterogeneous nucleation [17]. However, the same hierarchical structure inducing the superhydrophobicity may also lead to water condensing on the surface, which significantly reduces the contact angle and increases the contact area [18, 19]. Other challenges include the size of the rough features on the surface, as larger features increase the probability for ice formation [20].

This master's thesis is a continuation of the work done by four masterstudents the last 3 years [1, 2, 21, 22], as well as the project work done by Vegard Hornes in the spring of 2015 [23] and by the author the fall of 2015 [3]. Raasok and Halvorsen optimized the hydrophobic agent for the top layer [21, 22], whereas Luneng and Moe worked on methods for inducing micro- and nanoroughness on the surface [1, 2]. Sandblasting of steel was found most efficient for creating the microstructure, and the deposition of silica nanoparticles gave the best nanostructure. Surfaces combining both a hierarchical structure and the hydrophobic coating gave contact angles above 150° , but there was still a problem of too high adhesion between the droplet and surface.

1.2 Aim of the Work

This work will continue the development of hydrophobic surfaces for anti-icing applications. The material system consists of sandblasted 316 steel substrates, coated with nanoparticles of size 200-250 nm and a hydrophobic top layer based on 1H,1H,2H,2H-perfluorooctyltriethoxysilane. Steel 316 substrates are used due to the wide industrial usage of this alloy [24], and two different microstructures will be induced by sandblasting. In this work the method for depositing nanoparticles and the hydrophobic coating will be optimized. Methods include dip coating, spray coating, spin coating and vapor deposition.

The surfaces will be characterized in terms of contact angle, contact angle hysteresis and roll-off angle, both in normal ambient conditions and in an environmental chamber where temperature and humidity can be controlled. Furthermore the surfaces will be tested under freezing conditions to determine their anti-icing properties. Testing will include determining the freezing temperature, finding the delay of ice formation at a certain temperature and determining their behavior under icing/de-icing cycles. The goal is to increase the understanding of which features that yield icephobic properties, how important surface structure is versus surface chemistry, and if there is a link between hydrophobicity and icephobicity.

Chapter 2

Theory

In the following chapter some relevant background information and an overview of discoveries and work done in the field will be given.

2.1 Superhydrophobicity

The following section is largely based on [3]. There are two requirements for a surface to be called superhydrophobic. First, the contact angle between the water droplet and surface must exceed 150° . Secondly, the contact angle hysteresis should be lower than 10° . In the following section relevant terms, such as the contact angle, will be explained and the surface properties governing superhydrophobicity will be given.

The *contact angle* (CA) on a perfectly flat surface is defined by Young's equation [25]

$$\cos\theta_Y = \frac{\gamma_{SV} - \gamma_{SL}}{\gamma_{LV}} \quad (2.1)$$

where θ_Y is the contact angle, γ denominates the interface tension at the solid-vapor (SV), solid-liquid (SL) and liquid-vapor (LV) interfaces, respectively. Figure 2.1 shows the relation between these interface tensions and the CA, denoted by θ .

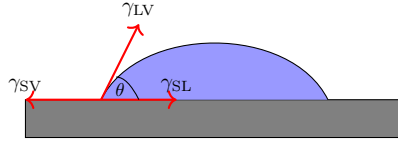


Figure 2.1: A droplet on a flat surface, relating the solid-vapor (γ_{SV}), liquid-vapor (γ_{LV}) and solid-liquid (γ_{SL}) interface tensions to the contact angle (θ).

Real surfaces are not perfectly flat, and several metastable states that differ slightly in energy can occur [26]. Each state corresponds to some CA. The span of stable states is often measured by tilting the surface, as illustrated in Figure 2.2. During tilting the droplet shape will change, until at some point the droplet moves. Just before movement the advancing and receding CA are found. The *advancing contact angle* (CA_{adv}) is the highest angle achievable on the surface, and the *receding contact angle* (CA_{rec}) is the lowest. The difference between these two is the *contact angle hysteresis* (CAH) of the surface.

$$CAH = CA_{adv} - CA_{rec}$$

The CAH is a measure of the adhesion between the droplet and the surface, and for superhydrophobic surfaces the adhesion should be as low as possible. Since CAH is measured by tilting the surface, the low CAH criterion can also be regarded as a low sliding angle or *roll-off angle* (ROA)¹ criterion [27].

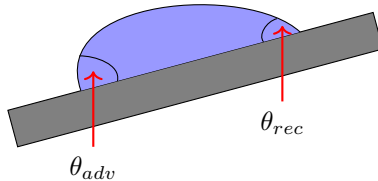


Figure 2.2: A droplet on a tilted surface showing the advancing, θ_{adv} , and receding, θ_{rec} , contact angles.

The largest CA achievable for a water droplet on a flat surface is 120° [28]. Surfaces showing CAs above 90° are called hydrophobic. However, the superhydrophobic requirement of CA larger than 150° is only achievable on rough

¹The angle of surface tilt causing the droplet to slide or roll-off the surface.

surfaces. There are two possible wetting states on rough surfaces, the Wenzel state and the Cassie-Baxter state, as shown in Figure 2.3.

In 1936 Wenzel described the wetting state where a droplet penetrates the rough features on a surface [29]. Wenzel's equation describes the apparent CA² on such a surface,

$$\cos\theta_W = r \cdot \cos\theta_Y \quad (2.2)$$

where r is the roughness factor of the given surface, and the contact angle θ_Y is given by Young's equation (2.1). r is defined by

$$r = \frac{\text{actual surface}}{\text{geometric surface}} \quad (2.3)$$

where the geometric surface is the surface as measured in the plane of the interface.

In 1944 Cassie and Baxter described the wetting state where a droplet rests upon a rough surface [30]. In the Cassie-Baxter state the apparent contact angle is given by

$$\cos\theta_{CB} = f \cdot \cos\theta_Y - (1 - f) \quad (2.4)$$

where f is the fraction of the interface area where the liquid is in direct contact with the surface. As the droplet traps air in the rough features, θ_{CB} can be seen as an average between the contact angle on a flat surface, and 180° (the contact angle with air).

By equating the apparent CA in the Wenzel and Cassie-Baxter states the threshold angle, θ_c , where both states can coexist is found [32]. θ_c is defined as

$$\theta_c = \frac{f - 1}{r - f} \quad (2.5)$$

where f is the fraction given in Equation 2.4 and r is the roughness defined in Equation 2.2. Droplets having a CA lower than θ_c are metastable in the Cassie-Baxter state. As a consequence applying pressure to such a drop can induce an irreversible transition to the Wenzel state. In this state more of the droplet is in contact with the surface, increasing the adhesion. To prevent such a transition the surface should be structured so that θ_c is minimized.

²The angle measured using a line parallel to the surface.

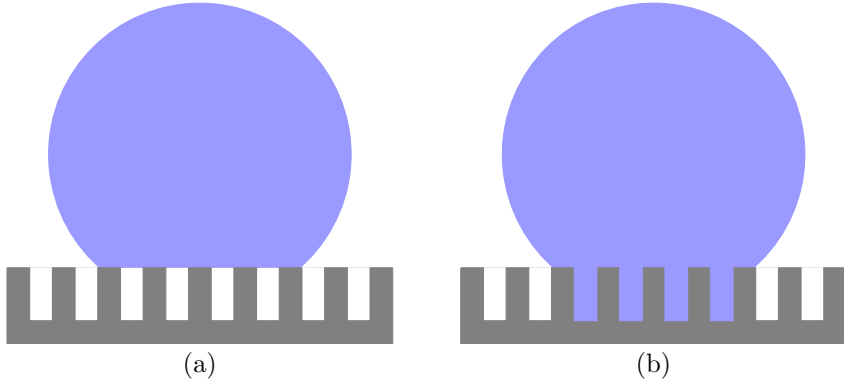


Figure 2.3: a) A droplet in the Cassie-Baxter wetting state, and b) a droplet in the Wenzel wetting state. Figure inspired by Antonini et al. [31].

2.1.1 The Lotus and Petal Effect

The lotus leaf is one of the most well known superhydrophobic surfaces found in nature, and the structure of the leaf has been widely studied [27, 33–35]. Two properties of the lotus leaf are important for the superhydrophobic character; the hierarchical structure and the low surface tension towards water. Roughness at a micro- and nanolevel makes up the hierarchical structure, whereas the chemistry of the leaf determines the surface tension. A combination of the two induces a surface in the Cassie-Baxter wetting state.

Another natural surface showing similar structure to the lotus leaf is rose petals. Here a third wetting state is observed, called the Cassie impregnating state [36]. The petal effect causes the grooves of the surface to be wet, whereas the plateaus are dry. A comparison of the lotus and petal effect is found in Figure 2.4. A characteristic of the petal effect is high adhesive forces, reported to be large enough for the water to stay attached even when the surface is turned upside down, which can be explained by the larger contact area between water and surface in this state.

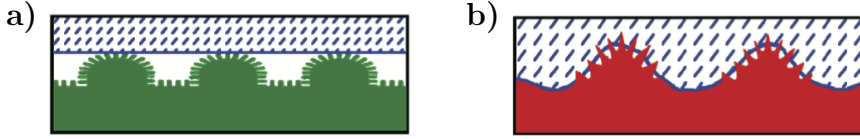
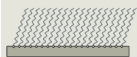




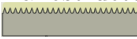
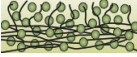
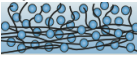


Figure 2.4: Illustrations of a) the lotus and b) the petal effect, adopted from Feng et al. [36]. The blue-spotted areas illustrate water on the surfaces.

2.2 Anti-Icing Surfaces

There are several strategies for creating anti-icing surfaces [6]. These include superhydrophobic surfaces with hierarchical surface roughness, smooth surfaces with self-assembled monolayers or bulk coatings, and wet surfaces that are structured, coated with infused polymer or hydrated. Table 2.1 gives an overview of the advantages and disadvantages of the different strategies. Dry surfaces have the ability to shed incoming water droplets, but there are issues with the humidity tolerance and durability, though improvements are made by the introduction of nanostructures. By the introduction of an aqueous lubricating layer the longevity can be improved since the lubricant can be replenished by atmospheric humidity, but there are still questions regarding the ice adhesion on such surfaces [37]. The introduction of slippery, liquid infused porous surfaces have shown high promise in terms of low ice formation from atmospheric humidity [38]. Under frosting conditions a superhydrophobic surface was found to be 90% covered in frost after 80 minutes, whereas the liquid infused surface only showed frost formation on 20% of its surface. Such surfaces have also shown very low ice adhesion [39]. The icephobicity of such surfaces can be compromised by a loss of the lubricant, and for increased lubricant retention an underlying nanostructure has been found important [40]. Further studies of all mentioned surfaces are required, especially with respect to properties under different environmental conditions [6]. In the following section more information on the anti-icing abilities of dry structures will be given.

Table 2.1: Advantages and disadvantages of strategies for making anti-icing coatings. Illustrations and content is adopted from Kreder et al. [6].

Type of surface	Advantages	Disadvantages
<i>Dry Surfaces</i>		
Self-assembled monolayer 	Environmentally tolerant	Limited compatibility and lower performance than state of the art
Bulk coatings 	Environmentally tolerant, versatile and durable	Lower performance than state of the art
Microstructured 	Rapid shedding of droplets prevent ice nucleation	Poor pressure and humidity tolerance, and poor durability
Nanostructured 	Improved pressure stability and improved humidity tolerance (jumping droplet effect)	Poor durability
<i>Wet Surfaces</i>		
Microstructured 	Low ice adhesion and droplet CAH, and high humidity and pressure tolerance	Poor resistance to lubricant depletion
Nanostructured 	Improved lubricant retention	Poor mechanical robustness
Infused polymer 	Increased lubricant content	Kinetics of lubricant depletion and replenishment unknown
Hydrated 	Low ice adhesion without need for lubricant replenishment	Poor wetting properties

An anti-icing surface should [41] :

- Prevent freezing of water condensing on the surface
- Prevent freezing of incoming water
- Have weak adhesion strength between ice formed and the surface

The ability to prevent freezing of water condensating on the surface can be measured by delay of icing, e.g. how long it takes for ice to form on the surface. Prevention of freezing incoming water depends on the ability to repel water droplets, especially at sub-zero temperatures. The last property will largely affect the energy required to remove ice [31]. For an airplane wing an anti-icing coating could mean that the air flow around the wings would be sufficient to remove ice.

The anti-icing properties of superhydrophobic surfaces are complicated, mainly because of the multiple length scales involved [6]. Typical superhydrophobic surfaces have a hierarchical structure, with roughness both at nano- and microlevel, ranging from 50 nm to 10 μm . The critical nucleus size for nucleation of ice is <10 nm and typical water droplets are in the microscopic range. In addition factors such as droplet impurities, surface chemistry and environmental conditions such as wind, temperature and humidity must be considered. There have been several studies on the correlation between hydrophobicity and anti-icing performance, and in the following sections some of these will be reviewed in terms of the three main properties of anti-icing surfaces.

2.2.1 Delay of Ice Formation

Delay of ice formation on superhydrophobic surfaces is generally attributed to the insulating effect of the air pockets found in a Cassie-Baxter state, the reduced contact area between surface and droplet, and to an increased free-energy barrier to heterogeneous nucleation [6]. The first two effects are directly related to the wetting state of the water droplet, as the less favorable Wenzel state corresponds to both the removal of air pockets and a larger contact area. The last property is a thermodynamic effect, which is evident for freezing of water. It is well known that the triple point for water is 0°C , however water without nucleation centers can be easily supercooled down to -41 - $(-42)^\circ\text{C}$ [42]. This temperature corresponds to the limiting temperature for homogeneous nucleation of water, and is mainly associated with the existence of an energy barrier for nucleation.

The freezing of a droplet on a surface will follow heterogeneous nucleation [43, 44]. At the surface - droplet interface the barrier for nucleation is lowered. The free energy barrier for heterogeneous nucleation is given by

$$\Delta G_{hetero}^* = \Delta G_{homo}^* \frac{(2 + \cos\theta)(1 - \cos\theta)^2}{4}. \quad (2.6)$$

θ is the contact angle between the droplet and surface, and ΔG_{homo}^* is the free energy barrier for homogeneous nucleation given by

$$\Delta G_{homo}^* = \frac{16}{3} \frac{\pi\gamma_{AB}^3}{\left(\frac{\Delta T}{T_m}\right)^2 \Delta H_f^2} \quad (2.7)$$

where γ_{AB} is the interfacial energy between phase A and B, ΔT is the temperature difference between the actual temperature of the system and the melting temperature, T_m , and ΔH_f is the latent heat of fusion. For superhydrophobic surfaces the barrier for heterogenous nucleation approaches that of homogeneous nucleation as

$$\frac{(2 + \cos\theta)(1 - \cos\theta)^2}{4}$$

approaches 1 when $\theta \rightarrow 180^\circ$, meaning that a larger supercooling (ΔT) is necessary for icing to occur. In addition to lowering the probability for heterogeneous nucleation, the reduction in contact area also reduces the heat transfer from the surface to the water droplet [17]. The ice nucleation delay for superhydrophobic surfaces was found to be more prominent at moderate degrees of water supercooling.

The hierarchical structure of superhydrophobic surfaces have shown delay in icing time [45], but whether this structure is the best for delaying ice formation has been questioned [13]. In the latter study surfaces with nanoscale roughness and higher wettability showed at least 1 order of magnitude longer icing delays than the surfaces with hierarchical roughness and lower wettability. Cao et al. [20] also illustrated the importance of lengthscale by making superhydrophobic surfaces from particle-polymer composites by mixing a binder with silica particles ranging from 20 nm to 20 μm . All the surfaces containing particles up to 10 μm in size were found to be superhydrophobic, both in terms of CA and CAH. When studying anti-icing properties it was found that the probability for ice formation remarkably increased for surfaces containing particles larger than 50 nm.

2.2.2 Repelling Impinging Droplets

Superhydrophobic surfaces have excellent water repellency and are therefore seen as good candidates for icephobic surfaces that repel incoming water droplets [6]. Under certain conditions droplets impinging on a superhydrophobic surface can retract and bounce off, due to the low CAH of the surfaces. Such behavior reduces the contact time between surface and droplet, and thus lower the probability for ice formation.

2.2.3 Ice Adhesion

Under extreme conditions ice will form even on the most icephobic surfaces, so the adhesion of ice already formed is an important property. The goal is to allow for passive ice removal, by factors such as wind or vibration. For this an ice adhesion below ~ 20 kPa has been set as a benchmark [6]. It should be mentioned that the coating also must have a good durability and high mechanical stiffness.

A study of 21 different coatings (200-300 nm thick) on flat steel showed that ice adhesion strength correlates strongly with the practical work of adhesion required to remove a liquid water drop from each test surface [46]. The work of adhesion is defined by

$$W_A = \gamma_{LV}(1 + \cos\theta_{rec}) \quad (2.8)$$

where γ_{LV} is the interface tension at the liquid-vapor interface and θ_{rec} is the receding contact angle. As mentioned above the largest contact angle achievable on a flat surface is 120° , setting a limit to the lowest adhesion possible on flat surfaces. Thus, further reduction of the ice adhesion strength requires a structured surface. A high CA_{rec} correlate with a low contact angle hysteresis, meaning that superhydrophobic surfaces are good candidates for achieving low ice adhesion.

Durability

Another important feature of anti-icing coatings is their durability during several icing/de-icing cycles. Surfaces with low CAHs have been found to have ice adhesion strength in the range 50-100 kPa, measured by applied shear stress in a centrifugal apparatus [12]. In a later study on the same material system the ice adhesion was found to increase with several icing/deicing cycles [18].

The initial values of 40-80 kPa increased to 180-200 kPa after 24 cycles. The authors attribute this to the deterioration of the nanostructure, leading to a larger contact area and a partial switch from the Cassie-Baxter state to a mixed Wenzel and Cassie-Baxter regime.

Farhadi et al. [47] showed that anti-icing abilities of the coating, exhibiting roughness at micro- and nanolevel, significantly deteriorated over several icing/de-icing cycles. The coatings were prepared by spin or dip coating, and consisted of organosilane, fluoropolymer or silicone rubber. Another study showed that stainless steel with surface modifications is robust against cyclic icing/deicing [14]. After 100 cycles the CA still exceeded 155° and the surfaces had maximum roll-off angles of 42° .

Atmospheric Humidity

A drawback for using superhydrophobic surfaces as anti-icing materials is their behavior under high atmospheric humidity. Problems like capillary condensation during vapor-oversaturation in the vicinity of superhydrophobic surfaces and the chemical stability of the hydrophobic agent under operating conditions have been addressed [42].

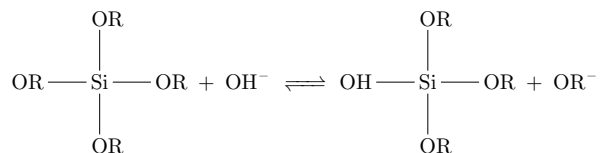
The CA of superhydrophobic surfaces have been shown to severely decrease under humid conditions [18]. A surface exhibiting a CA of 152° was kept on a cooling stage at -2°C for 90 minutes in ambient atmosphere, which reduced the CA to 130° . Another study investigated the energy needed to keep ice from forming [31]. Under low liquid water content (LWC) the superhydrophobic coating lead to a 80% energy reduction compared to an untreated surface. However, under high LWC conditions the reduction was only 10%.

2.3 Sol-Gel Synthesis

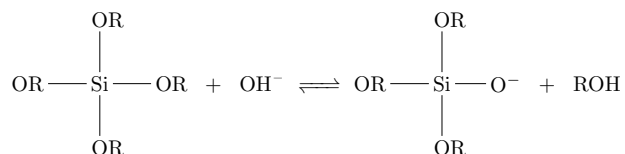
Sol-gel synthesis is a common way for creating coatings on surfaces. A sol of colloidal particles³ is deposited and forms a gel⁴ upon gelation. The process can be divided into six general steps [48]:

1. Formation of a stable precursor solution.
2. Gelation by polycondensation or polyesterification reactions.
3. Aging (also called syneresis). Continuation of the polycondensation reactions until the gel transform into a solid mass, accompanied by contraction of the network and expulsion of the solvent.
4. Drying. Water and other volatile liquids are removed from the gel network.
5. Dehydration. Removal of surface-bound M-OH groups. Normally achieved by calcination.
6. Densification and decomposition of the gel at high temperatures (>800°C).

The formation of a sol starts with a precursor, which often is alkoxide-based. One example is tetraethyl orthosilicate (TEOS), which can be written as $\text{Si}(\text{OR})_4$. The first reaction is hydrolysis, which can happen under basic or acidic conditions. Under basic conditions the following reaction happens:



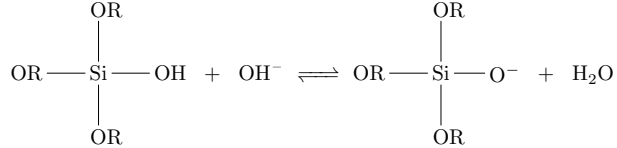
After, and in parallel with the hydrolysis, condensation reactions occur. As with hydrolysis, condensation can occur under basic or acidic conditions. At high pH the condensation can start with the base activating an original precursor molecule,



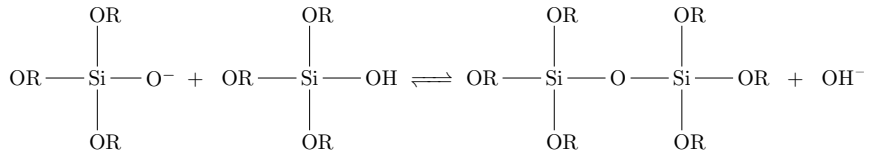
³A dispersion of solid particles with diameter 1-100 nm.

⁴A interconnected, rigid network with submicron pores and polymeric chains longer than one micrometer.

or with a reaction between a hydrolyzed molecule and the base



followed by a condensation reaction



2.3.1 Water Content

The amount of OR-groups that are replaced by OH-groups depend on the water to silicon ratio. The magnitude of $n = \frac{\text{H}_2\text{O}}{\text{Si}}$ is important for the final morphology since OH^- is a slightly better leaving group than OR^- . n around 1 will lead to the formation of dimers, for n around 2 longer chains or two-dimensional rings can form, and higher water content lead to the formation of three-dimensional fractals.

2.3.2 pH

Another factor influencing the final structure is pH. Low pH promotes the formation of chains, whereas high pH induces particle growth. Under basic conditions the stability of the transition state in the hydrolysis reaction, and consequently the rate of hydrolysis, increase with water content. So high pH will further promote the formation of fractals, or particles. Given time these particles will aggregate, so short growth times is important for particle formation. Figure 2.5 illustrates how pH and growth time affects the final product.

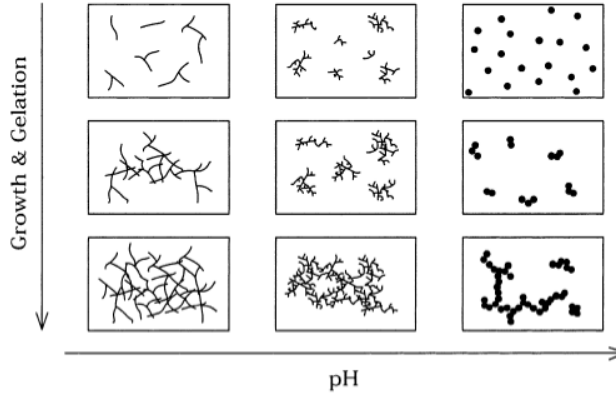


Figure 2.5: Scheme showing the effect of pH on the gel structure. Figure adopted from Cushing et al. [48].

2.3.3 Formation of Particles

Silica *nanoparticles* (NPs) are usually grown by the *Stöber-Fink-Bohn* (SFB) method [49]. The method involves hydrolysis of TEOS in an ethanolic medium in the presence of a base, such as ammonia. The particle formation in the SFB method has been investigated by several authors [50–52]. The formation of monodisperse particles in the SFB method can be explained by a classical nucleation and growth model [50]. Particles grown by this mechanism will have a uniform, amorphous inner volume.

However, studies have shown the structure of silica particles to be porous [50,52]. Due to this a second mechanism has been proposed, illustrated in Figure 2.6. Subparticles up to several nanometers in size aggregate to form larger particles. At some point during the growth the mechanism changes to monomeric addition, leading to smooth particles with dense shells. The overall reaction conditions determine when the change in mechanism occurs. Other studies of the growth kinetics support this mechanism, as the concentration of silica precursor was found to be above the critical limit [52]. This suggests that nuclei are created continuously and the result should be a broad range of particle sizes. As the SFB-method is known for its monodispersity, the most plausible explanation is that the small particles aggregate and form larger particles.

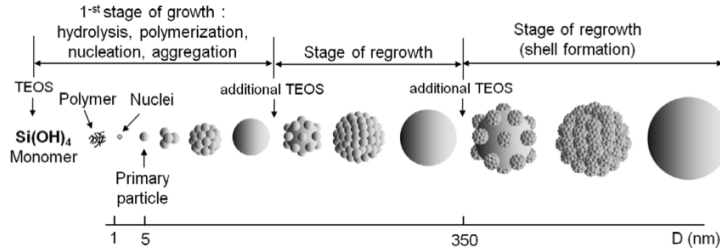


Figure 2.6: Mechanism for particle growth by multistage growth in TEOS hydrolysis in alcohol-water-ammonia solution. Adopted from Masalov et al. [50].

2.3.4 Fluorosilane

A superhydrophobic surface needs to have the right surface chemistry, and one way to achieve this is by deposition of molecules containing fluorinated carbon chains. Long carbon chains are known to be hydrophobic, and the addition of fluoromolecules increases this effect. The low *critical surface tension* (γ_c) of surfaces covered by such chains is a measure of the hydrophobicity [53]. A liquid with surface tension lower than γ_c will completely wet the surface ($\theta_Y=0$), and surfaces with γ_c lower than 35 dynes/cm² are generally hydrophobic [28]. Fluorinated carbon chains show γ_c around 20 dynes/cm² [53]. An example of molecules containing such chains are fluorosilanes, which can be deposited by several methods [28].

2.4 Deposition Techniques

There are several ways for depositing a sol on a substrate. These include spray coating, dip coating and spin coating. Coatings can also be deposited without starting from a sol, as is the case for vapor deposition.

2.4.1 Dip Coating

The *dip coating* (DC) process can be divided into five stages: immersion, start-up, deposition, drainage and evaporation [52]. The substrate to be coated is vertically immersed into a coating bath where the formation of a film starts. After some time the substrate is withdrawn at a constant speed resulting in the deposition and drainage of the film, and evaporation of the solvent. In a successful dip coating process the condensed phase remains dispersed in the solute, macroscopic gelation is avoided, and the sol is sufficiently dilute so that the critical cracking thickness is not exceeded. Figure 2.7 shows a schematic of the process.

When the withdrawal speed is low, and the liquid viscosity is low, the thickness of the film is given by

$$t_w = 0.94 \frac{(\eta U_0)^{2/3}}{\gamma_{LV}^{1/6} (\rho g)^{1/2}}, \quad (2.9)$$

where η is the viscosity, U_0 denotes the withdrawal speed, γ_{LV} is the interface tension between the liquid and air, ρ is density of the sol and g is the gravitational constant. At this thickness, t_w , there is a balance between the viscous drag ($\propto \frac{\eta U_0}{h}$), gravitational force ($\rho g h$) and the surface tension (γ_{LV}).

During drying the solvent will evaporate and pores in the structure will collapse, yielding a thinner film. The thickness of the dry film can be written as

$$t_d = \frac{\rho - \rho_s}{\rho_p - \rho_s} t_w \quad (2.10)$$

where t_w is given by Equation 2.9, ρ_s is the density of the solvent and ρ_p is the density of the dry film.

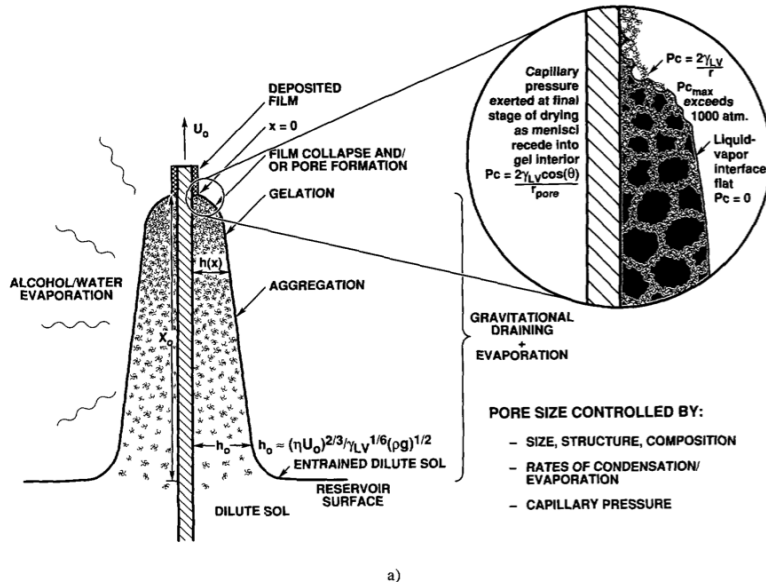


Figure 2.7: Schematic of the steady-state dip coating process. Figure adopted from Brinker et al. [54].

2.4.2 Spray Coating

Several authors have used *spray coating* (SC) to produce superhydrophobic surfaces [55–57]. In SC the sol to be deposited is mixed with a carrier gas and sprayed onto the substrate through a nozzle [58]. Heat can be applied to the substrate if desired. Figure 2.8 shows a schematic of the process. SC offers several advantages over dip coating. It is faster, the waste of coating sols is smaller, coating sols with rather short pot lives can be used and the coating step is suitable for establishing an in-line process.

The film formation is affected by how the droplet lands on the surface, and the film morphology is affected by the substrate temperature, the precursor solution, the size of the droplets, the spray rate and the pressure of the carrier gas [59, 60]. How thick the sprayed film becomes depends on the distance between the spray nozzle and substrate, the temperature, the concentration of the solution and the quantity of precursor sprayed.

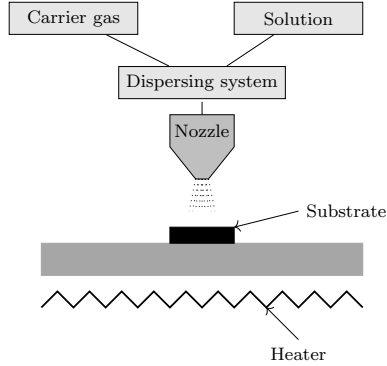


Figure 2.8: Schematic of spray coating equipment. The sol and a carrier gas is mixed and sprayed onto the substrate, which can be heated to evaporate the solvent faster. Figure inspired by Attia et al. [58].

2.4.3 Spin Coating

The *spin coating* (SPC) process contains four stages; deposition of the sol, spin-up, spin-off and gelation by solvent evaporation [52, 58]. Figure 2.9 shows a schematic of the four stages. In the deposition stage an excess of liquid is dispensed on the surface, which is radially drawn outwards during spin-up due to the centrifugal force. During spin-off excess liquid flows to the perimeter of the sample and leaves as droplets. The rate of removal decreases with thinning of the films, as the resistance to flow increase. In the last step the film is thinned further by evaporation.

The thickness of an uniform film during spin-off is described by

$$h(t) = \frac{h_0}{(1 + 4\rho\omega^2 h_0^2 t / 3\eta)^{1/2}} \quad (2.11)$$

where h_0 is the initial thickness, t is time, ρ is density, ω is the angular velocity and η is liquid viscosity. ρ and ω are assumed constant. The most important parameters influencing the thickness and microstructure of a spin coated film is the rotating speed, the viscosity of the sol and the wetting properties between the sol and substrate [61, 62].

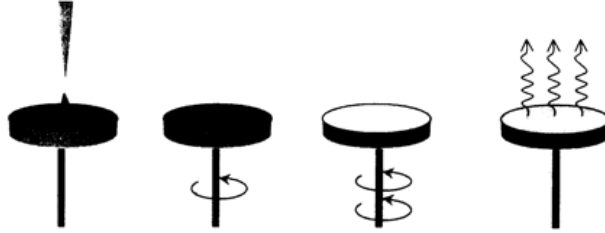


Figure 2.9: Schematic diagram of the stages of the spin coating process: deposition of the sol, spin up, spin off and gelation by solvent evaporation. Adopted from Attia et al. [58].

Bonding of Sol Molecules

The molecules in the sol applied by SC, SC or SPC can appear as dimers, chains or fractals depending on the parameters in the sol-gel process, as described in Section 2.3. In these molecules or clusters of molecules there will be unreacted OH-groups which can form bonds to the OH-groups on the surface to be coated. Figure 2.10 illustrates how such a bonding process can occur.

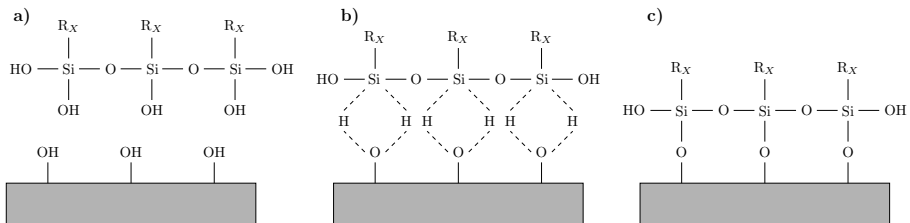


Figure 2.10: Schematic of how bonding can occur between a chain of hydrolyzed precursor molecules from the sol-gel and the surface containing hydroxy groups. R_X represents, in the case of a fluorosilane, a carbon chain where most of the hydrogens are replaced by fluor. a) Initial state before bonding occurs. b) Formation of hydrogen bonds between the hydroxy groups at the surface and the hydroxy groups on the silane chain. c) Formation of a chemical bond.

2.4.4 Vapor Deposition

Vapor deposition (VD) is the process of making a thin film from the condensation of gas molecules on a surface [63, 64]. The molecules are supplied from an external source, and are vaporized by heat or vacuum (or both). One example of molecules that can be deposited in this way are silanes [28]. VD of silanes favor monolayer deposition. In order to form bonds between the silanes and surface extended reaction times (4-12 hours) and elevated temperatures (50 - 120°C) are typically applied.

The coverage of silanes achieved on the surface depends both on the surface chemistry and on the silane precursor used. For the surface the concentration and type of hydroxyl groups, the hydrolytic stability of the bond formed and the physical dimensions of the substrate or substrate features are important. The best substrates are silica, quartz and glass. When an organofunctional silane reacts with such a surface a substitution reaction at the silicon occurs, resulting in a covalent bond to the surface through an oxygen. How reactive the silane is depends on the leaving group. In order of decreasing reactivity Si-NR_2 is more reactive than $\text{Si-NH-Si} > \text{Si-O}_2\text{CCH}_3 > \text{Si-OCH}_3 > \text{Si-OCH}_2\text{CH}_3$. Other important factors include the volatility of byproducts and the steric bulk of the groups. Methoxy- and ethoxysilanes are most widely used.

Chapter 3

Experimental

Stainless steel 316 substrates were sandblasted (SB) and cleaned by isopropanol. Nanoparticles (NPs) were made by Stöber-Fink-Bohn (SFB) method and deposited on the SB substrates to obtain a hierarchical surface structure with both nano- and microroughness. Lastly, a β -silane coating was put on top through a sol-gel process or directly from the precursor by vapor deposition (VD). The samples were characterized in terms of surface structure and chemistry by SEM, profilometer, contact angle (CA) measurements and icing experiments. The experimental procedure used is illustrated by the flow chart in Figure 3.1.

3.1 Substrate Treatment

In the following section details on the substrates, parameters for sandblasting and details on the cleaning procedure will be given.

3.1.1 Substrate

The substrates used were 316 stainless steel substrates precut into 2x10x15 mm pieces by NTNU Finmekanisk verksted. The 316 alloy consists of 10-14% Ni, 16-18% Cr, 0.08 % C, 2% Mn, 0.75% Si, 0.03% S, 0.045% P, 0.10% N, Mo 2.0-3.0% and Fe to balance.

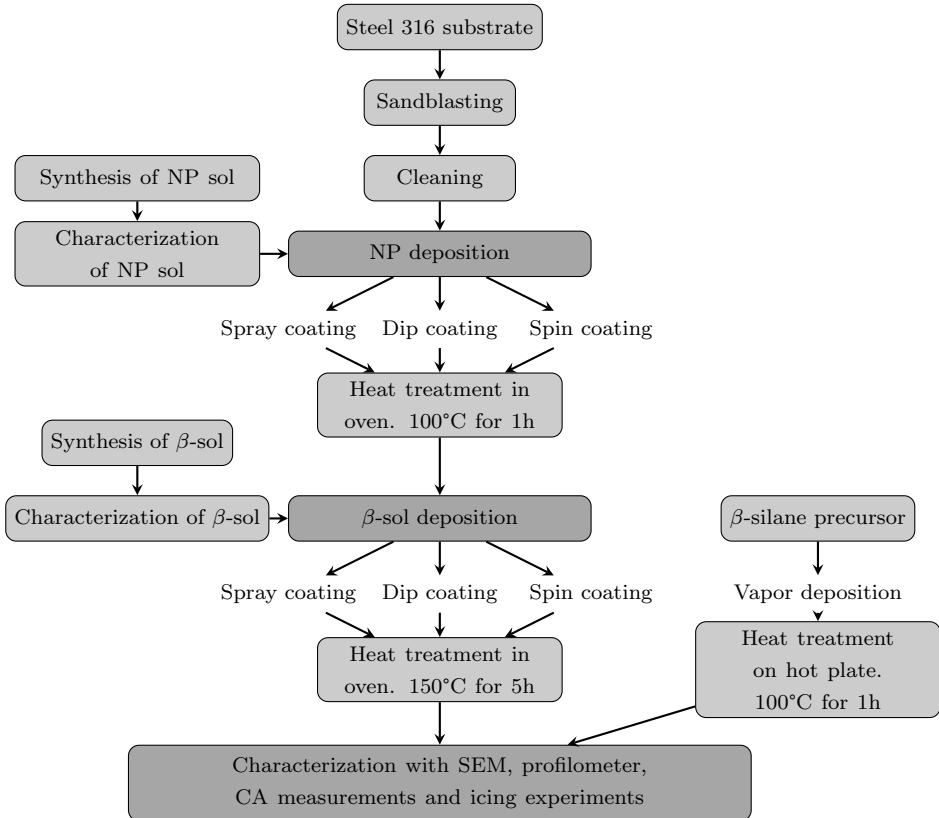


Figure 3.1: Flow chart of the experimental procedure.

3.1.2 Microroughness

Sandblasting was used to induce microroughness on the steel substrates. Two different types of sand, of different size and chemistry, were used. The first was SiO_2 with a mean size of $150\ \mu\text{m}$ and the second was Al_2O_3 in the size range $500 - 1000\ \mu\text{m}$ (from SprayService, type NK-I).

The sandblasting was performed in the sandblasting cabinet belonging to SINTEF (in the "Verkstedteknisk" building). To ensure only one sand type was present during sandblasting the cabinet was cleaned using pressurized air be-

fore and after each procedure. The small substrates were attached to a plank using duct tape, to ensure they were not lost in the process. Sandblasting was performed for about 5 seconds on each substrate, keeping the nozzle at a distance of approximately 5 cm. The sand was ejected using pressurized air, but the exact amount of ejected material and pressure is unknown.

3.1.3 Cleaning

The substrates were cleaned by a 24 hour soak in isopropanol (2-propanol from VWR, CAS number 67-63-0). Substrates dried in normal atmosphere and were coated with nanoparticles (or a mix of both NPs and β -silane) immediately after drying.

3.2 Synthesis of Silica Nanoparticles

Silica NPs were made by a SFB method, using tetraethyl orthosilicate (TEOS) as precursor and ethanol as a solvent. A schematic of the TEOS molecule is shown in Figure 3.2. NPs were produced using a protocol adopted from earlier work by Luneng [1]. In addition to TEOS and ethanol, water was added as reaction agent and an ammonium hydroxide solution induced basic conditions. Table 3.1 shows the chemicals used.

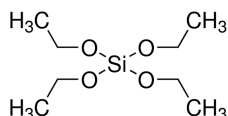


Figure 3.2: Schematic of tetraethyl orthosilicate. Adopted from [65].

Particles were made by first mixing ethanol, distilled (DI) water and NH_4OH in a 100 mL round bottom flask. The flask was attached to a condenser and placed on a RCT Basic dry block heater (IKA) at 35 °C, under 300 rpm of magnetic stirring. After 10 minutes TEOS was added dropwise to the solution, and the solution was left to react for 60 minutes, still at 300 rpm and 35 °C. The exact amounts of chemicals used can be found in Appendix A.1.

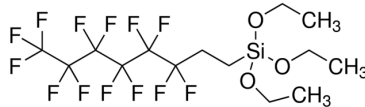
Table 3.1: Chemicals used for synthesizing particles and their function.

Name	Chemical formula	Provider	CAS	Function
Tetraethyl orthosilicate	$\text{Si}(\text{OC}_2\text{H}_5)_4$	Sigma-Aldrich	78-10-4	Precursor
Ammonium hydroxide solution (28-30 %)	$\text{NH}_4\text{OH}(\text{aq})$	Sigma-Aldrich	1336-21-6	Catalyst
Ethanol	CH_3OH	VWR	64-17-5	Solvent

The NP-sol was cooled down to room temperature and immediately used for coating steel substrates. The remaining sol was stored at 5 °C in glass containers.

3.3 Coating Preparation

The hydrophobic sol was made by a sol-gel method using 1H,1H,2H,2H-perfluorooctyltriethoxysilane (β -silane) as a precursor. Figure 3.3 shows a schematic of the molecule.

**Figure 3.3:** Schematic of 1H,1H,2H,2H-perfluorooctyltriethoxysilane. Adopted from [66].

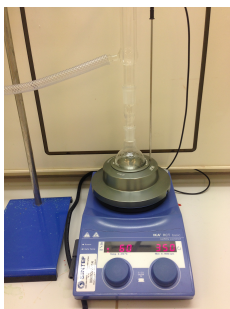
The protocol used for preparing the sol was adapted from earlier work [1,2], and utilized the chemicals listed in Table 3.2.

The sol content can be written as β -xR-yS-E-10. β expresses β -silane being the precursor, R is the molar ratio of water to β -silane, S is the molar ratio of solvent to β -silane, E stands for ethanol being the solvent and 10 is the pH used. x and y indicate the molar ratios used, and for this work x was equal to 3 and y was equal to 40 or 5. From now on the β -3R-40S-E-10 sol will be called β -40S-sol and the β -3R-5S-E-10 sol will be called β -5S-sol.

Table 3.2: Chemicals used for synthesis of the β -silane sol and their function.

Name	Chemical formula	Provider	CAS	Function
1H,1H,2H,2H-perfluorooctyl-triethoxysilane	$C_{14}H_{19}F_{13}O_3Si$	Sigma-Aldrich	51851-37-7	Precursor
Ammonium hydroxide solution (28-30 %)	NH_4OH	Sigma-Aldrich	1336-21-6	Catalyst
Ethanol	CH_3OH	VWR	64-17-5	Solvent

NH_4OH was added to DI water to achieve pH 10. The water was mixed with precursor and solvent in a 50mL round bottom flask according to the ratios defined above. The flask was placed on a RCT Basic dry block heater from IKA at 60°C and 350 rpm, attached to a condenser and left to react for 60 minutes. Figure 3.4 shows a picture of the set up used. The finished sol was cooled down to room temperature and immediately used for coating. Unused sol was stored at 5°C in glass containers. Details on the amount of chemicals used for producing the β -sols can be found in Appendix A.2.

**Figure 3.4:** Image of the set up used for sol-gel synthesis. A round bottom flask containing the sol was connected to a condenser and placed on a RCT Basic dry block heater from IKA.

3.4 Deposition Techniques

In this work silica NP-sol was deposited by spray coating (SC), dip coating (DC) and spin coating (SPC). The β -silane was either deposited in a sol by DC or SC or directly by VD.

3.4.1 Dip Coating

DC was performed by a KSV DC X2 Dip Coater from KSV Instruments. The substrate, SB 316 steel, was held in place by a clip, and a special teflon holder was filled with sol. About 2 mL of sol was used, filling the holder to the top. The holder was placed directly underneath the substrate. Figure 3.5 shows an image of the equipment used.

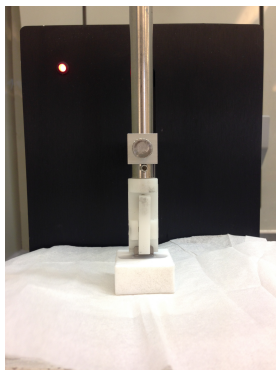


Figure 3.5: Image of dip coating process showing the KSV DC X2 Dip Coater, the sample being held by the clip and the teflon solution holder.

DC was performed by immersing the substrate at the highest possible speed (170 mm/min), holding the substrate in the solution for 10 minutes and withdrawing at the lowest possible speed (5 mm/min). The substrate was left in the clip for two minutes after dipping to allow the solvent to evaporate. The same program was used for applying NP-sol, β -40S-sol or β -5S-sol.

3.4.2 Spray Coating

SC was performed by an Exacta-coat automatic spray coater from Sono-Tek. The system included a syringe filled with solution connected to a nozzle through plastic tubes, where it was mixed with the N_2 carrier gas supplied at 5 bar. A SonicSyringe stage moved the plunger on the syringe, and volume dispensed was controlled by SyringePump software. The syringe could also be connected to an ultrasound source, allowing for in situ mixing of the spraying liquid. The spraying procedure was controlled by the software Pathmaster which allowed control of spray direction, distance between lines, speed of the nozzle and number of layers being applied. Figure 3.6 shows an image of the system.

Prior to spraying the system was rinsed with isopropanol. Then the syringe was filled with the spraying sol, and the tubing was flushed to ensure that there was no isopropanol left in the system. The program was made to cover an area of 20x30 mm to avoid edge effects on the 10x15 mm substrates. The nozzle moved in a line pattern across the substrates, covering it with solution in one or several layers. When applying several layers, the line patterns crossed each other.

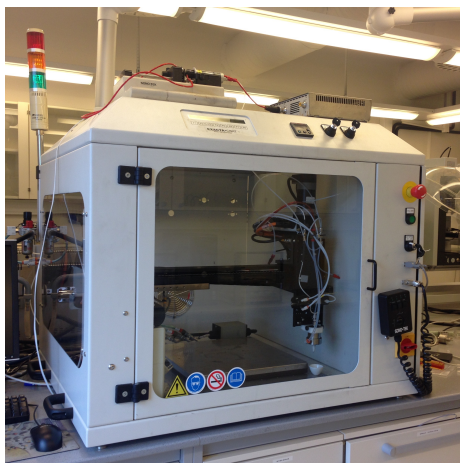


Figure 3.6: The Exacta-coat automatic spray coater.

Nanoparticle Deposition

The NP-sol was sprayed in one layer. The tip speed was 40 mm/s with 3 mm distance between the lines. Table 3.3 shows the different amounts used.

Table 3.3: Parameters used for NP-sol deposition by SC.

Program	Amount dispensed
SC1	0.1 mL/min
SC2	0.5 mL/min
SC3	1.0 mL/min

β -sol Deposition

The β -40S-sol was typically applied in several layers. The tip speed was 40 mm/s and the line spacing 3 mm. Prior to spraying the β -40S-sol was diluted with 100% ethanol (from VWR, CAS 65-17-5) and the solution was mixed by magnetic stirring at 350 rpm for 10 minutes. To shorten the drying time between layers the substrates were subjected to 50°C heat, which was found sufficient for the layer to dry in a few minutes. Table 3.4 shows the different parameters used.

Table 3.4: Parameters used for β -40S-sol deposition by SC.

Program	Amount dispensed	Dilution	Layers	Heat
β -SC1	0.5 mL/min	1:3	1	-
β -SC2	0.5 mL/min	1:3	2	-
β -SC3	0.5 mL/min	1:1	2	50°C

Nanoparticle and β -sol Deposition

NPs and β -40S-sol were also sprayed in one step, as fewer steps would be beneficial for industrial applications. The NP-sol and β -40S-sol was synthesized as described in Sections 3.2 and 3.3, respectively. The β -40S-sol was made first,

and kept in the fridge while the NP-sol was synthesized. Equal volumes of the two sols were mixed in a round bottom flask at 300 rpm magnetic stirring for 15 minutes, and then immediately used for spraying. The spraying programs used are summarized in Table 3.5.

Table 3.5: Parameters used for one step NP and β -40S-sol SC.

Program	Amount dispensed	Layers	Heat
Combo1	0.5 mL/min	1	-
Combo2	0.5 mL/min	2	-
Combo3	0.1 mL/min	4	50°C
Combo4	0.5 mL/min	4	50°C

3.4.3 Spin Coating

SPC was performed by a WS-400B-6NPP/LITE/AS spin coater from Laurell Technologies. The substrate was loaded onto the chuck and vacuum hold-down was engaged from the control panel. NP-sol was dispensed manually on the substrate by a pipette. The spin speed, acceleration and time was programmed, and the parameters used are shown in Table 3.6. The spin-up step was set to 10 seconds, whereas the spin-off lasted for 30 seconds.

Table 3.6: Parameters used for SPC of NP-sol.

Program	Spin-up acceleration	Spin-off speed
SPC1	136 rpm/s	500 rpm
SPC2	136 rpm/s	800 rpm

Heat Treatment

After deposition of both NPs and β -sol by one of the above methods the substrates were heat treated in a Carbolite HT-/28CR oven. The NP-sol was heat treated at 100°C for 1 hour, with a heating and cooling rate of 50°C/hour. After deposition of β -sol the substrates were heat treated at 150°C for 5 hours, using

the same heating and cooling rates. When NPs and β -sol were applied in one step, the samples were only heat treated at 150°C for 5 hours.

The lowest temperature achievable in the oven was 54°C, and the lack of cooling element lead to the real cooling rate being lower than 50°C/hour. Thus, to start heat treatment at room temperature the oven had to be turned off for some time. Also, a steeper cooling rate was achieved by opening the oven at the end of the program.

3.4.4 Vapor Deposition

VD was done in a desiccator. A sample and a beaker containing β -silane was placed in the desiccator, and vacuum was applied to vaporize the β -silane. A few droplets of β -silane was sufficient. Figure 3.7 shows the equipment used and in a) the desiccator is seen. To make sure that the desiccator was filled with silane molecules a pumping cycle of 3 times 5 minutes was applied, with the chamber being sealed for 10 minutes between each pumping. The pumping cycle was adopted from earlier work by Moe [2]. After the last pumping the chamber was sealed for deposition. Parameters used are shown in Table 3.7. In program β -VD4 extra pumpings were applied after the first sealing time, each lasted 5 minutes followed by an hour of sealing.

Table 3.7: Parameters used for VD of β -silane.

Program	Sealing time	Subsequent pumping	Subsequent sealing time
β -VD1	1 h	-	-
β -VD2	14 h	-	-
β -VD3	22 h	-	-
β -VD4	14 h	2 x 5 min	1 h

After silanization the samples were put on a Heidolph MR Hei-Standard hot plate at 100 °C for one hour to ensure binding between the β -silane molecules and the sample surface. Figure 3.7 b) shows a picture of the hotplate used, with a sample on top. This was an essential step since the deposition was done at room temperature, and deposition of silanes typically is done at elevated temperatures [28].

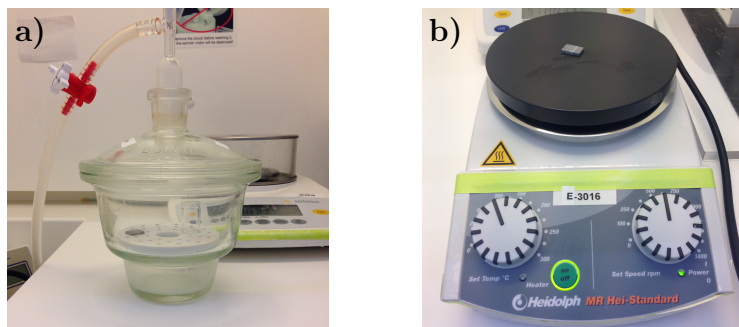


Figure 3.7: Equipment used for vapor deposition. a) The desiccator used for vapor deposition of β -silane. The small glass beaker contains the precursor. b) The hot plate used for heat treatment with a sample on top.

3.4.5 Overview of Samples Made

Table 3.8 shows an overview of the samples made in this work, with the parameters for each step specified and a sample ID with abbreviations summing up each sample. The samples were SB with either fine (F) or coarse (C) sand. Two rounds of sandblasting were performed with each type and for the coarse sand this resulted in two different roughnesses, C and C1. To achieve a hierarchical structure nanoparticles were deposited by SC, DC or SPC. The hydrophobic surface chemistry was achieved by depositing β -40S-sol by DC or SC, β -5S-sol by DC, or by depositing β -silane directly by VD. In Section 3.4 details on the parameters used in each step can be found, and the abbreviations used in the sample IDs refer to the programs described there.

Table 3.8: Overview of samples made in this work. The substrates were SB with either fine (F) or coarse (C) sand. The coarse sand resulted in two different roughnesses (C and C1). Nanoparticles were deposited by SC, DC or SPC. β -silane was deposited through a sol by DC or SC, or directly from the precursor by VD. Details on the programs used can be found in Section 3.4.

SB	Nanoparticle deposition	β -silane deposition	Sample ID
F	0	0	F
C	0	0	C
C1	0	0	C1
F	0	DC	F- β -DC
C	0	DC	C- β -DC
C	SC [0.1 mL/min]	DC	C-SC1- β -DC
F	SC [0.5 mL/min]	VD [1h]	F-SC2- β -VD1
C	- -	- -	C-SC2- β -VD1
F	- -	DC	F-SC2- β -DC
C	- -	- -	C-SC2- β -DC
C	SC [1.0 mL/min]	SC [(1:1), 0.5mL/min x2]	50°C, C-SC3- β -SC3
F	- -	- -	F-SC3- β -SC3
F	- -	DC	F-SC3- β -DC
F	- -	VD [14 h]	F-SC3- β -VD2
F	- -	DC, β -5S	F-SC3- β -5S-DC
C1	- -	- -	C1-SC3- β -5S-DC
F	- -	VD [22 h]	F-SC3- β -VD3
C1	- -	VD [14+1+1 h]	C1-SC3- β -VD4
F	- -	SC [(1:3), 0.5mL/min x2]	F-SC3- β -SC2
F	DC	SC [(1:3), 0.5 mL/min]	F-DC- β -SC1
F	- -	VD [22 h]	F-DC- β -VD3
F	SPC [500 rpm]	DC	F-SPC1- β -DC
F	SPC [800 rpm]	- -	F-SPC2- β -DC
F	SC NP and β [0.5mL/min]		F-Combo1
F	SC NP and β [0.5mL/min x2]		F-Combo2
F	SC NP and β [0.1mL/min x4, 50°C]		F-Combo3
F	SC NP and β [0.5mL/min x4, 50°C]		F-Combo4

3.5 Characterization

The substrates were characterized in terms of surface structure by SEM and profilometer, the sols were characterized by viscosity measurements and the final surface structures were characterized by contact angle measurements and icing experiments.

3.5.1 Electron Microscopy

Scanning Electron Microscopy (SEM) imaging was done by a Zeiss Supra field-emission SEM. Typical parameters used were acceleration voltage of 5 kV, 8 mm working distance and 30 μm aperture. SEM was used for characterizing the roughness after sand blasting, as well as for looking at the distribution of nanoparticles and coating on the rough surface.

The thickness of NP coatings was also determined by SEM. Prior to imaging the samples were mounted into Polyfast, a conducting thermoplastic from Struers. 22.5 mL of Polyfast was distributed around the sample placed vertically in the chamber of a LaboPress-1 from Struers. Hot mounting was performed by heating at 180°C and 15 kN pressure for 4 minutes and then water cooling in 2-3 minutes. When the thermoplastic had cooled the sample was ground until the sample was seen and buffed before imaging.

SEM images were also used for characterization of the silica nanoparticle size. The diameter was measured of about 100 particles in one image taken at relatively high magnification by using the software ImageJ [67, 68]. For detection of β -silane film on the surfaces *back-scattered electrons* (BSE) was detected. To get enough signal the aperture size had to be increased to 60 μm .

3.5.2 Viscosity Measurements

Viscosity of the sols used was measured by HAAKE RheoWin MARS III from Thermo Scientific immediately after synthesis. The same measurement program was used both for the NP-sol and β -sols. Measurements were conducted at 20 °C under constant shear rate using approximately 2 mL of sol. The program used is described in Table 3.9. During the first step the speed was increased linearly, before it was kept constant in the second step where the measurements were conducted, and lastly the speed was linearly decreased.

Table 3.9: Program used for measuring viscosity of synthesized sols.

Program	Shear Rate [1/s]	Time[s]	Number of Measurement Points
Rot Ramp (step)	0.01000 - 500.0	180	100
Rot Time	500.0	30	100
Rot Ramp (step)	500.0 - 0.01000	180	100

3.5.3 Profilometer

The roughness induced by sand blasting was investigated by a Veeco Dektak 150 profilometer. Two samples of each type were measured with three scans across each sample. The stylus used had a radius of 12.5 μm and applied a force of 3.00 mg. Each scan lasted for 60 seconds and measured over a length of 1000 μm or 800 μm . The measurement range was set to 65.5 μm with "Hills and Valleys" mode enabled. The average roughness, R_a , of each scan was automatically calculated by the software.

3.5.4 Contact Angle Measurements

CAs were measured using a Drop Shape Analyzer - DSA100 from Krüss, shown in Figure 3.8. Sessile drop mode was used and the liquid was DI water. To calculate static CAs the Young-Laplace fitting model was used. CA measurements were generally performed under normal ambient conditions.

Programming of experiments and calculation of contact angles were done in Advance software. The sample table height was adjusted so that the sample could be seen on the screen, and the sample was placed directly under the dispensing needle. A high speed camera recorded the droplet and brightness, zoom, focus and frame per second could be adjusted. When camera settings were set the image on the screen was calibrated using the known size of the droplet dispensing needle. In this way the droplet size was controlled both by the dispensing syringe and the camera screen. Measurements were done by either recording a video or by taking multiple measurements at given time intervals.

The baseline for measurements could be set automatically, but as this often was found to be unstable the baseline was mostly set manually. Using the same



Figure 3.8: The DSA100 from Krüss used for contact angle measurements.

baseline for a series of measurements also reduced the variation. For measurements of static CAs the program was set to do 10 measurements during the first 5 seconds after deposition of a droplet, and an average of the 10 measurements was taken. Three different areas on each sample was tested. The droplet size was $8\ \mu\text{L}$. Figure 3.9 a) shows an image of a typical droplet and the measured CA.

The roll-off angle (ROA) was measured by tilting of the instrument. A $8\ \mu\text{L}$ droplet was deposited and the entire instrument was tilted at a rate of $60^\circ/\text{min}$ until the droplet moved or completely rolled off. If the roll-off angle was lower than 90° , an exact measure of the ROA was made by taking multiple measurements once or twice per second during tilting. The ROA was defined as the tilting angle when the droplet moved and the contact angle hysteresis (CAH) was measured at the same point using the Tangent fitting mode. Figure 3.9 b) shows an example of a CAH measured.

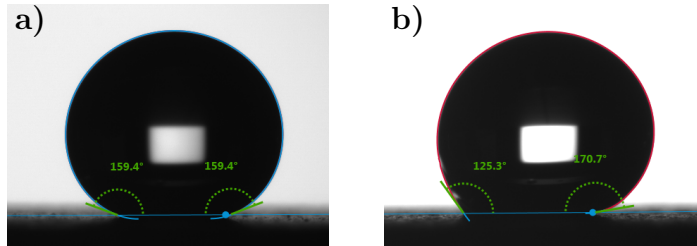


Figure 3.9: Droplets on flat and tilted surfaces. a) Image showing a droplet on a typical sample surface. The software fitted the droplet with the blue circle using the Young laplace fitting mode and calculated the CA on each side based on the surface set by the blue baseline. b) CAH measured just before roll-off. The red line shows the fitting of the droplet in the Tangent mode and the CA on each side is calculated.

3.5.5 Environmental Experiments

CAs were also measured under controlled environmental conditions to see the effect of temperature and humidity on the coatings. Such measurements were performed in a TC40 environmental chamber connected to a HC10 humidity chamber mounted on the DSA100. A front view of the TC40 chamber can be seen in Figure 3.10. A separate thermostat controlled the temperature supported by a Julabo F12-MA refrigerate and heating circulator, and a Silver-Line L-S20 compressor supplied gas to the HC10.

The samples were placed in the chamber, inside an extra heat conducting hood, and the wanted temperature and humidity was set by the thermostat and Advance software, respectively. A temperature sensor recorded the real temperature in the chamber. The sample was typically subject to the given conditions for 5 minutes before a 8 μL droplet was deposited and the CA was measured as described in Section 3.5.4.

In icing experiments the HC10 had to be turned off, as it could not withstand temperatures below 5°C. To get a measure of how the humidity developed in these experiments, a preliminary experiment was performed. This was done by emptying the HC10 for water and shutting off the gas supply, so that it would not affect the humidity but still be able to record it. The waterbath was set

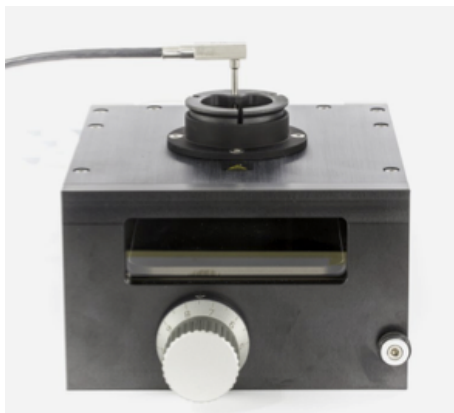


Figure 3.10: Front view of TC40 environmental chamber, with the temperature sensor inserted on top.

to 2°C. The chamber was opened to ambient conditions and then sealed. The humidity was recorded at the start, and then the temperature was lowered at the course of 5 minutes down to 5°C. The new humidity at this temperature was recorded immediately, and after 5 and 10 more minutes.

3.5.6 Icing Experiments

Icing experiments were also performed in the TC40 environmental chamber mounted on the DSA100. As the HC10 did not withstand sub-zero conditions it was disconnected. For freezing experiments the Julabo circulator was set to 2°C. Experiments included measurements of the energy barrier for ice formation, the time for ice formation, cyclic behavior and studies of the mechanism.

Energy barrier for Ice Formation

The energy barrier for ice formation was measured by depositing a droplet on the sample at 5°C and then gradually lowering the temperature. Samples were held at 5°C for 5 minutes before a 8 μ L droplet was deposited. The CA was measured and then the temperature was lowered at approximately 1°C/min. When 0°C was reached the cooling was recorded, and the exact temperature required for

freezing was noted. Figure 3.11 shows images of a typical icing process. The image in Figure 3.11 a) is taken just before the droplet freezes, and in b) the black center indicates the start of ice formation. In Figure 3.11 c) the droplet has froze solid, indicated by the pointy tip at the top. The volume of the droplet increased from a) to c).

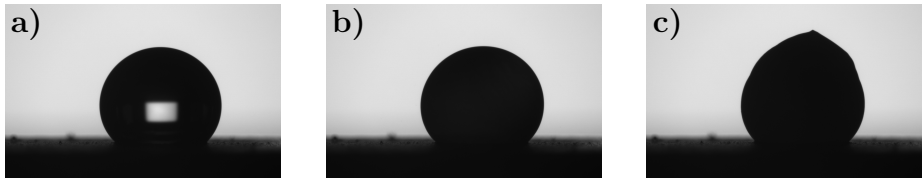


Figure 3.11: Pictures showing the freezing process. a) The droplet just before the freezing starts, which is shown in b). From b) to c) the volume increased.

Delay of Ice Formation

The delay of ice formation was measured at -10°C . This temperature was set based on the results of the energy barrier measurements. The samples were cooled down to -10°C and held there for 5 minutes before a $8\ \mu\text{L}$ droplet was deposited and the time before the droplet froze was recorded.

Cyclic Icing Behavior

One of the main challenges for anti-icing coatings is their durability through several icing/de-icing cycles. As a primary measure of this some of the samples showing the highest and lowest freezing temperature were put through three cycles of icing and de-icing. A $8\ \mu\text{L}$ droplet was deposited at room temperature and then cooled down $1^{\circ}\text{C}/\text{min}$ until the droplet froze, followed by a heating of $1^{\circ}\text{C}/\text{min}$ until it was completely liquid. The droplet was held at $+5^{\circ}\text{C}$ for 5 minutes before the process was repeated two more times.

Chapter 4

Results

In the following chapter the surface structure obtained on steel 316 substrates, the hydrophobic character of the coatings, and their behavior under different environmental conditions in addition to their icing characteristics will be presented.

4.1 Microroughness

Table 4.1 shows the average roughness obtained by sandblasting with two different types of sand, measured by a profilometer. Three scans across 1000 μm on two samples gave an average roughness of $3.6 \pm 1.0 \mu\text{m}$ for the coarse 500 - 1000 μm sand, and $1.6 \pm 0.2 \mu\text{m}$ for the fine 150 μm sand.

The reproducibility of the method was tested by measuring the roughness of another batch of sandblasted (SB) substrates. Three scans across 1000 μm gave an average roughness of $5.5 \pm 1.4 \mu\text{m}$ for the coarse sand and $1.4 \pm 0.2 \mu\text{m}$ for the fine sand. The two batches SB with fine sand showed similar roughness. These were considered to have the same surface structure, the fine structure or simply F. The larger deviations by the coarse sand resulted in two structures, C and C1. Figure 4.1 show the difference in roughness obtained by the two different types of sand, by plotting the topography from an F sample in the

same diagram as a C topography. Figure 4.1 a) shows the result for a 1000 μm scan and b) an 8000 μm scan.

Table 4.1: Surface roughness obtained by sandblasting with two different types of sand. Two samples of each type was measured with three lines on each sample, where both a detailed scan over 1000 μm and an overview scan over 8000 μm were performed.

SB	Roughness [μm] across 1000 μm	Roughness [μm] across 8000 μm
Coarse (C)	4.3 ± 0.8	4.8 ± 0.2
Coarse (C)	2.9 ± 0.8	3.6 ± 0.9
Fine (F)	1.7 ± 0.3	1.6 ± 0.2
Fine (F)	1.45 ± 0.03	1.59 ± 0.06

4.2 Coating Characterization

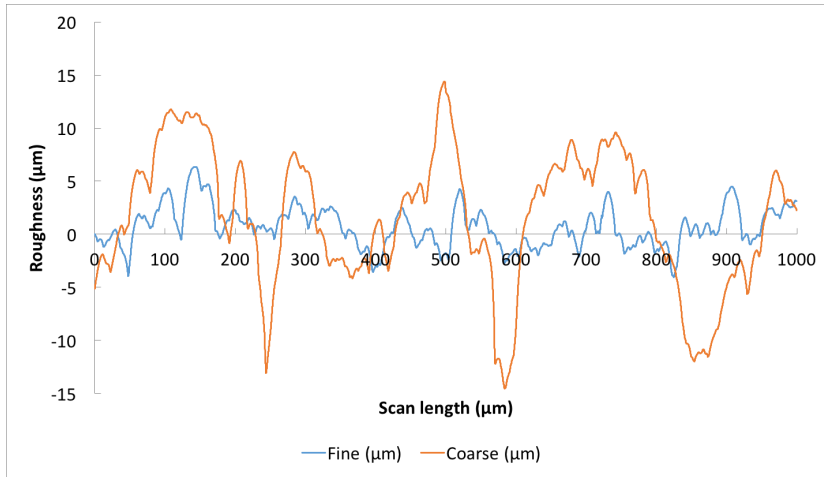
4.2.1 Nanoparticle Size

In Figure 4.2 the surface structure of sample F-SC2- β -DC is shown. The steel surface had an F microstructure and nanoparticles (NPs) were spread out on the surface. The particles were spherical in shape and appeared monodisperse. Analysis by ImageJ on 100 particles in the left part of the image gave an average particle size of 261 nm with a standard deviation of 26 nm.

4.2.2 Rheological Properties

Table 4.2 shows the measured viscosity of the sol produced, as well as calculated densities. Densities were calculated using the material properties in Appendix A.1 and A.2. The reported viscosity was averaged over 100 measurements taken at constant shear rate. The viscosity of the β -5S-sol was measured in an earlier work [3], and was approximately twice of the β -40S-sol viscosity.

a)



b)

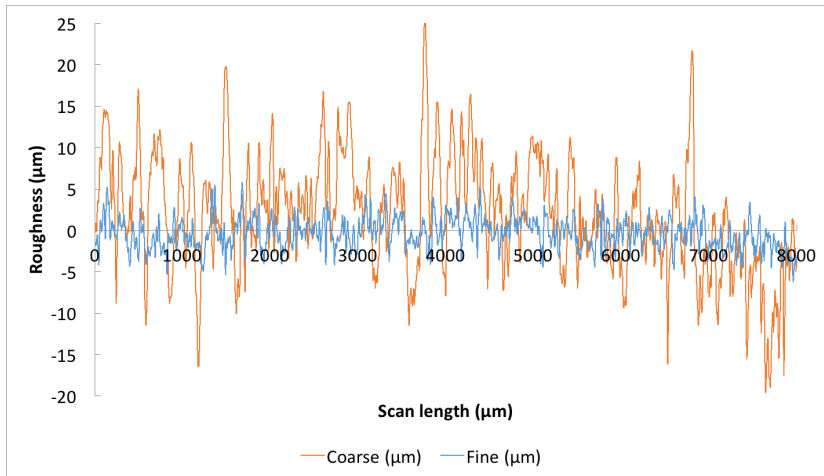


Figure 4.1: Comparison of profilometer scans of across a fine and coarse structure; a) Scans across 1000 μm and b) scans across 8000 μm . The blue lines indicate the fine surface topography, whereas the coarse is shown in orange.

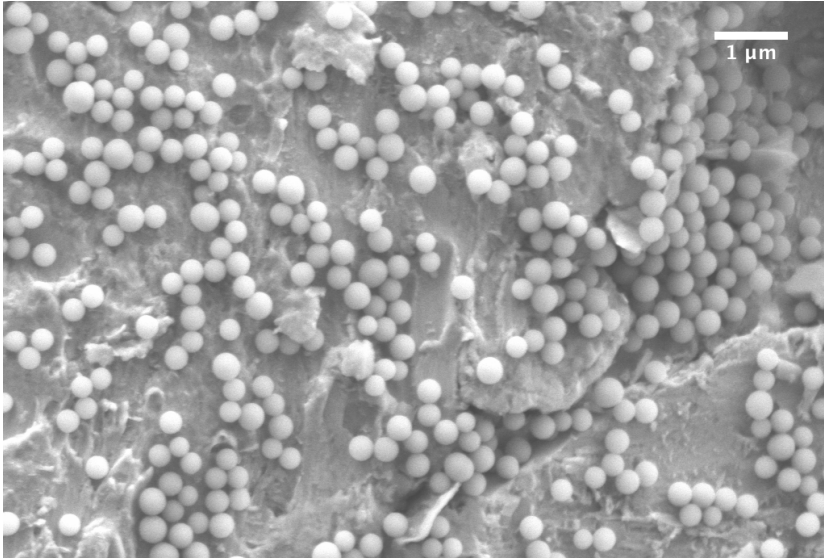


Figure 4.2: SEM image of F-SC2- β -DC used for determining particle size. The steel surface had a fine microstructure, and spherical nanoparticles were spread across the surface.

Table 4.2: Viscosity and calculated densities of produced sols.

Sol	η [mPa·s]	Density [g/mL]
NP	1.92 ± 0.05	0.819
β -40S	1.59 ± 0.05	0.868
β -5S [†]	3.14 ± 0.01	1.089

[†] The viscosity was measured in an earlier work [3].

4.3 Nanoroughness

The obtained nanoroughness on the surfaces by the different coating methods will be presented in this section.

4.3.1 Dip Coating

NP deposition by dip coating (DC) gave variable results. Though the protocol and NP-sol used was the same, the coverage varied from thick deposits to more distributed particles. There was always a thick line present where the meniscus of the sol was during immersion. Lines also had a tendency to form further down on the substrate perpendicular to the dipping direction. Figure 4.3 shows a SEM image of a surface sandblasted with fine sand and covered with NPs by DC. A line of thick deposits can be seen, marked by a red outline, whereas around this line the particles were more evenly spread.

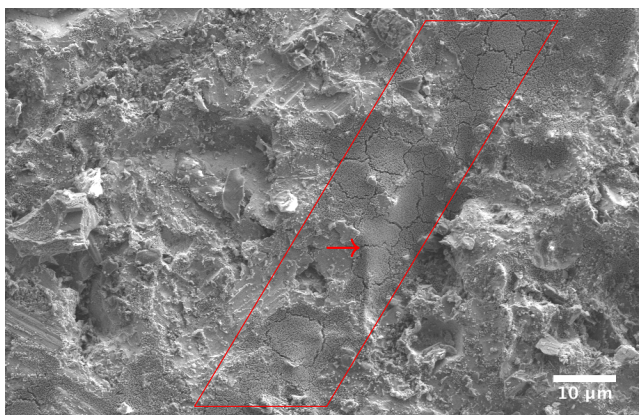


Figure 4.3: SEM image of a fine steel substrate dip coated with NPs. A line of thick NP deposit is marked by the red outline. The red arrow points to one of the cracks forming as a result of the thick deposit of NPs.

To get an idea of just how thick the deposits forming on dip coated samples were, a cross-section of a dip coated C sample was made. Figure 4.4 shows an image of one area of the cross-section where the thickest NP deposits were

found. The gray area in the bottom is the steel substrate, and the black at the top is the Polyfast thermoplastic used for casting. By measuring 10 vertical lines along this section the thickness was found to be $8.9 \pm 0.5 \mu\text{m}$, corresponding to about 34 NPs stacked on top of each other. The red arrows in Figure 4.4 show examples of two such lines.

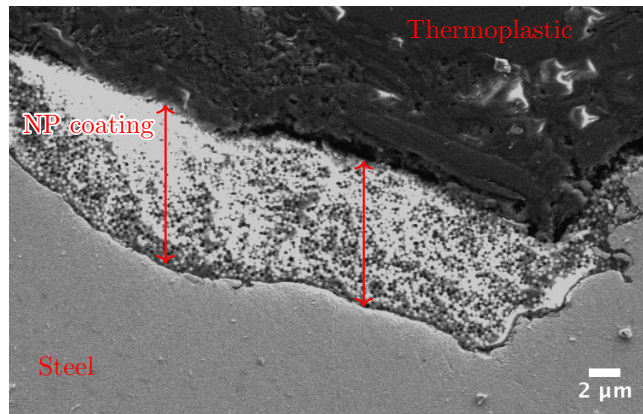


Figure 4.4: Cross section of a dip coated coarse sample, showing an area covered by several layers of NPs. The sample was mounted in a thermoplastic before making the cross-section. The gray area in the bottom is the steel substrate, and the black at the top is the thermoplastic. The red arrows show how the thickness of the cross-section was measured.

4.3.2 Spray Coating

The deposited amount was varied for spray coating (SC). Figure 4.5 shows the surface obtained by SC with 0.1 mL/min in a) and 0.5 mL/min in b). Figure 4.6 shows the surface obtained when spraying with 1.0 mL/min. The surface in Figure 4.5 a) had a C microstructure, whereas the two others had F microstructures. Using 0.1 mL/min resulted in nanoparticles spread out on the surface, either as single particles or in clusters of a few particles. Increasing the amount to 0.5 mL/min gave a more even coverage, and some areas appeared to be covered in several layers of particles. 1.0 mL/min gave an even more dense coverage, and areas with cracking in the NP-film appeared.

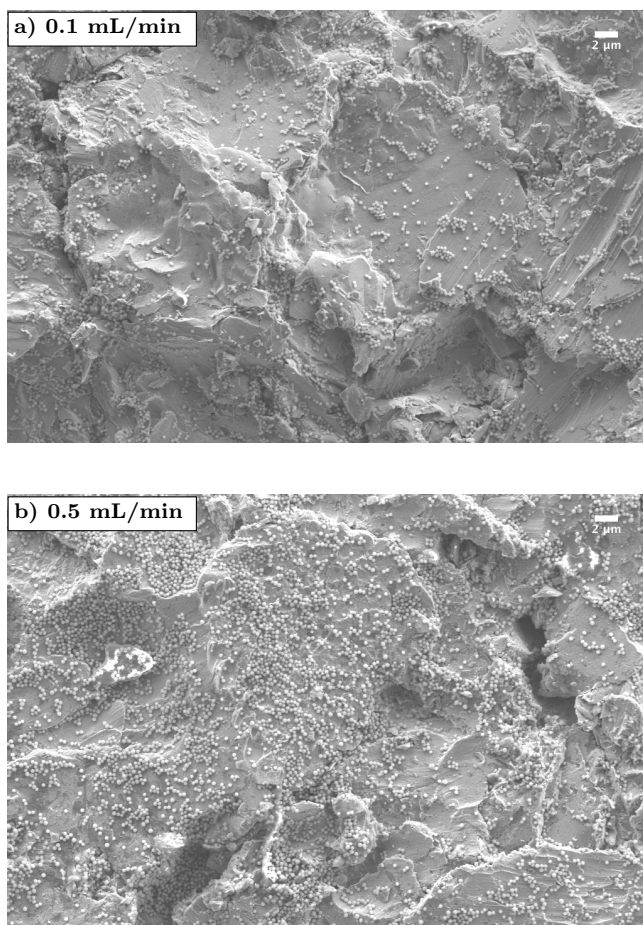


Figure 4.5: SEM images of spray coated surfaces. a) A surface sprayed with 0.1 mL/min nanoparticle sol and b) the result for 0.5 mL/min. The surface in a) had a coarse microstructure and in b) a fine microstructure is seen.

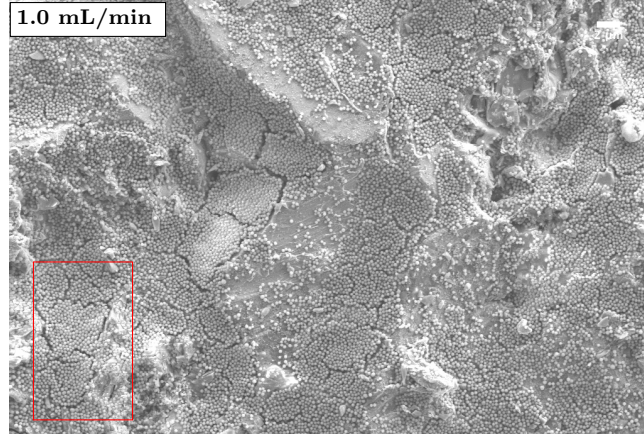


Figure 4.6: SEM image of spray coated surface. Spray coating was performed with 1.0 mL/min on steel with a fine microstructure. The red rectangle marks an area with thick NP deposits, causing the film to crack.

4.3.3 Spin Coating

The spin speed was varied for spin coating (SPC), and Figure 4.7 and 4.8 show SEM images of surface structures obtained. In Figure 4.7 the result for SPC at 500 rpm is shown. The image was taken in the middle of the sample. Figure 4.8 shows the result for 800 rpm. Figure 4.8 a) show the surface in the middle of the sample, whereas the image in b) was taken towards the edge of the sample. The thickness increased when moving towards the edges of the samples. In Figure 4.8 b) areas with thick NP deposits, causing cracking in the film, are seen. No such areas were found in the middle of the sample, as in the example shown in Figure 4.8 a).

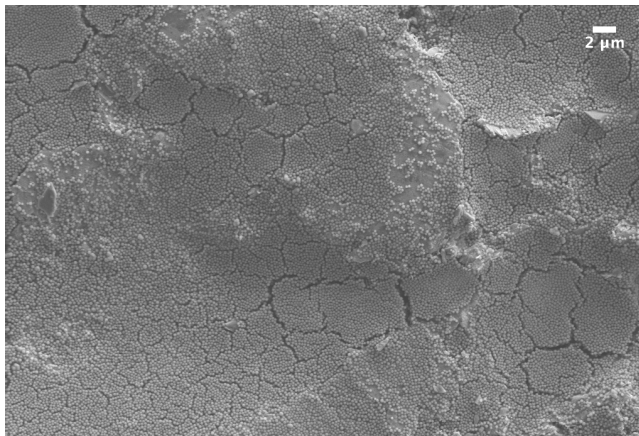


Figure 4.7: SEM image of the surface obtained by 500 rpm SPC of NP-sol. The surface was SB with fine sand.

4.4 Wetting and Adhesion of Water Droplets

Table 4.3 shows all the contact angles (CAs) measured. For samples showing a CA above 150° , the measured roll-off angle (ROA) and contact angle hysteresis (CAH) are included. The reported values are averages of at least three measurements, including the calculated standard deviations. The CAs of SB samples and SB samples coated with only β -40S-sol are included as references.

4.4.1 Effect of Nanoparticle Deposition

As shown in Table 4.3 both NPs and β -silane must be deposited to achieve both a CA larger than 150° and a low ROA/CAH. The best sample was F-SC3- β -5-DC showing a CA of $158 \pm 2^\circ$, ROA of $8 \pm 2^\circ$ and CAH of $19 \pm 3^\circ$. When no NPs were deposited, the CAs still exceeded 150° , but the ROAs were higher than 90° and the samples showed high CAHs.

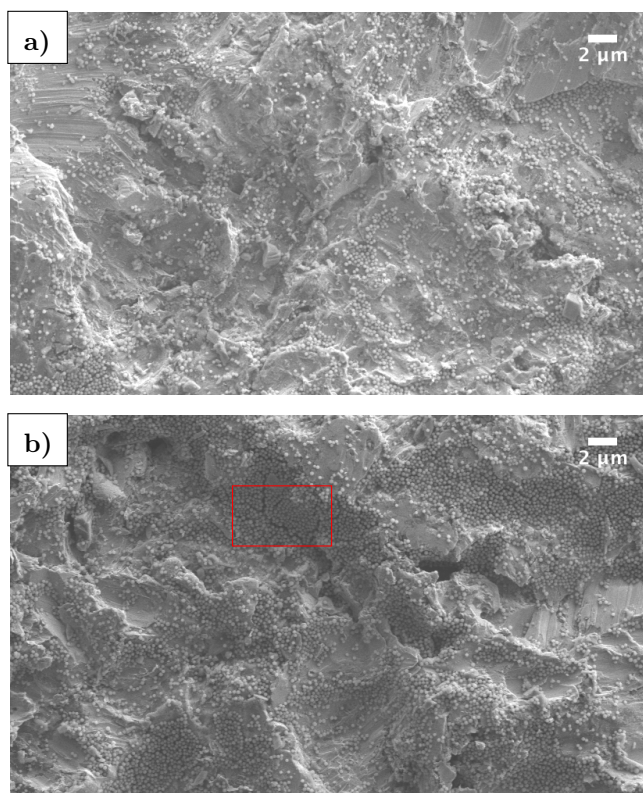


Figure 4.8: Surface structure obtained by SPC of nanoparticles. The steel was sandblasted with fine sand, the acceleration was 136 rpm/s, the spin time 30 seconds and the spin speed 800 rpm. a) The surface obtained in the middle of the sample, and b) surface obtained towards the edge of the sample. The red rectangle in b) marks an area with thicker NP deposits.

Table 4.3: CAs, ROAs and CAHs achieved in this work. Information on how each sample was made can be found in Table 3.8. The droplet size was 8 μ L.

Sample ID	CA [°]	ROA [°]	CA _{adv} [°]	CA _{rec} [°]	CAH [°]
F	62 ± 5	N/A	N/A	N/A	N/A
C	77 ± 5	N/A	N/A	N/A	N/A
C1	100 ± 3	N/A	N/A	N/A	N/A
F- β -DC	153 ± 2	> 90	160 ± 11	103 ± 7	57 ± 10
C- β -DC	151 ± 2	>90	168 ± 3	96 ± 7	73 ± 8
C-SC1- β -DC	150 ± 2	>90	161.9 ± 0.3	104 ± 11	72 ± 7
F-SC2- β -VD1	126 ± 4	>90	N/A	N/A	N/A
C-SC2- β -VD1	136 ± 6	>90	N/A	N/A	N/A
F-SC2- β -DC	163 ± 3	20 ± 4	175 ± 4	125 ± 7	50 ± 4
C-SC2- β -DC	163 ± 3	13 ± 3	171 ± 2	134 ± 3	37 ± 5
C-SC3- β -SC3	157 ± 4	18 ± 10	165 ± 4	128 ± 23	28 ± 10
F-SC3- β -SC3	156 ± 3	15 ± 2	161 ± 2	136 ± 1	26 ± 2
F-SC3- β -DC	164 ± 4	9 ± 1	178 ± 1	136 ± 2	41 ± 2
F-SC3- β -VD2	140 ± 3	>90	N/A	N/A	N/A
F-SC3- β -5S-DC	158 ± 2	8 ± 2	166 ± 3	147 ± 1	19 ± 3
C1-SC3- β -5S-DC	157 ± 1	10 ± 3	167 ± 3	135 ± 14	32 ± 20
F-SC3- β -VD3	139 ± 1	>90	N/A	N/A	N/A
C1-SC3- β -VD4	147 ± 1	>90	N/A	N/A	N/A
F-SC3- β -SC2	156 ± 1	52 ± 21	173 ± 1	96 ± 4	80 ± 5
F-DC- β -SC1	154 ± 3	21 ± 14	172 ± 5	117 ± 2	56 ± 2
F-DC- β -VD3	117 ± 5	>90	N/A	N/A	N/A
F-SPC1- β -DC	157 ± 1	16 ± 3	172 ± 3	140 ± 3	32 ± 5
F-SPC2- β -DC	153 ± 4	>90	169 ± 1	97 ± 4	72 ± 5
F-Combo1	153 ± 3	>90	162.4 ± 0.5	93 ± 3	70 ± 3
F-Combo2	151 ± 1	>90	157 ± 2	94 ± 1	63 ± 3
F-Combo3	151 ± 2	>90	171 ± 3	98 ± 3	72 ± 3
F-Combo4	121 ± 1	>90	N/A	N/A	N/A

4.4.2 Effect of β -silane Deposition

Figure 4.9 illustrates the best CA and ROA achieved by the different methods for β -silane deposition on fine substrates. The samples were coated with an equal amount of NPs, achieved by SC with 1.0 mL/min. For VD a higher CA was achieved on the C1-SC3- β -VD4 sample, but the ROA still exceeded 90°.

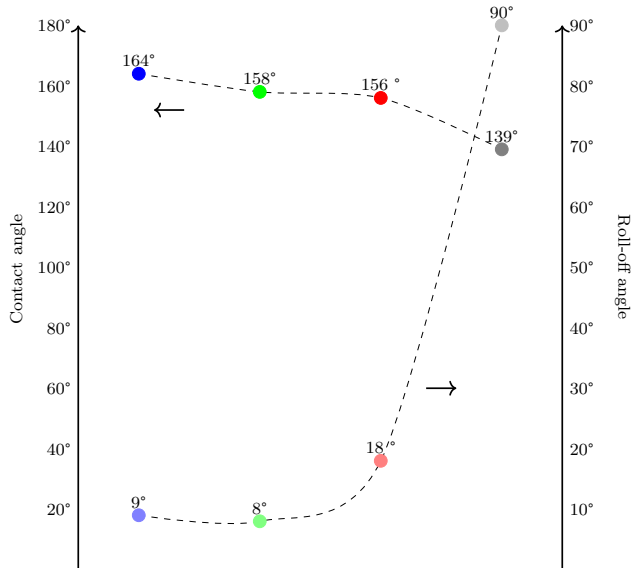


Figure 4.9: Average contact and roll-off angles achieved with different coating methods for the β -silane. By DC (β -40S-sol ● and β -5S-sol ●), by SC (●) and by VD (●). Substrates had a F microstructure and nanoparticles were deposited by SC using 1.0 mL/min. CAs are in stealth colors and ROAs in faint colors.

Samples that showed high CA and low ROA were assumed to be covered by β -sol. On such surfaces features believed to be broken pieces of a thicker β -silane film, or dense agglomerates, appeared. Figure 4.10 shows an example of such a surface. Figure 4.10 a) shows a SEM image acquired in SE mode, whereas 4.10 b) shows the result from BSE mode. The features believed to be film are marked by red rectangles, and appear light in Figure 4.10 a) and dark in Figure 4.10 b). No such features appeared on the samples where β -silane was deposited by VD.

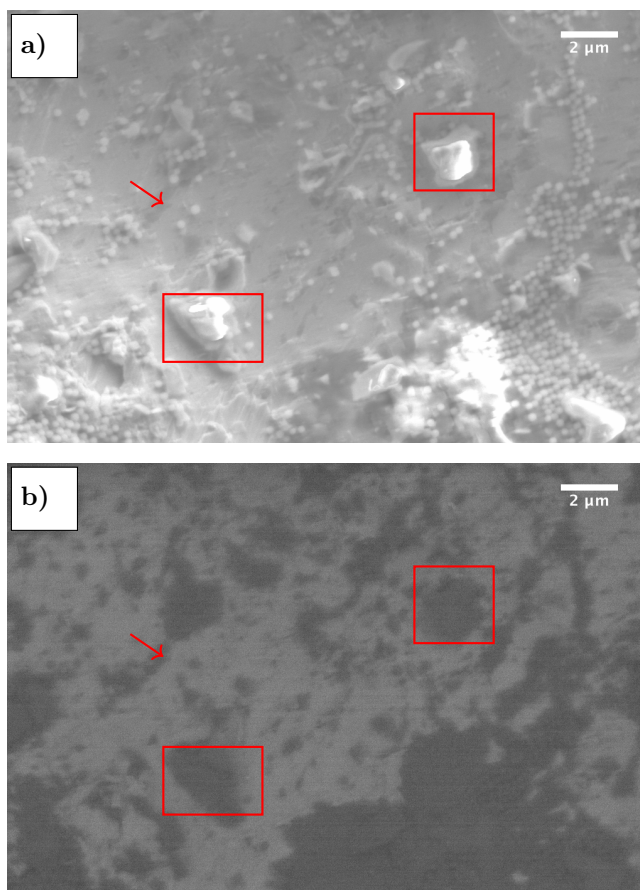


Figure 4.10: SEM images taken in a) SE mode and b) BSE mode on the same area on sample F-SC3- β -5S-DC. The red rectangles mark features believed to be β -silane film. The red arrow marks a crack in the surface, which was dark in both modes.

4.4.3 Combined Nanoparticle and β -silane Deposition

It was challenging to achieve even surface coverage by one step SC of both NP-sol and β -40S-sol. SEM of the surfaces revealed areas with dense coverage of NPs, and other areas covered by almost no particles. Figure 4.11 shows examples of surface structures obtained by this method. The image in Figure 4.11 a) was taken on F-Combo1, whereas Figure 4.11 b) shows the surface of F-Combo4. In Figure 4.11 a) only half of the surface shown is covered by NPs.

For the case of F-Combo3 the pattern from the SC could be seen on the sample by the naked eye, suggesting that the spray cloud was too small when the sprayed amount was reduced down to 0.1 mL/min. A more even coverage was attempted by increasing the amount and layers applied, which resulted in the surface of F-Combo4 seen as in Figure 4.11 b). This surface appeared flatter than the other surfaces produces, and also had a much lower CA. The thick films seen on the surface is believed to be β -silane. F-Combo1, F-Combo2 and F-Combo3 all showed CA around 150° , whereas F-Combo4 only gave a CA of $121 \pm 1^\circ$. All the samples showed ROAs larger than 90° .

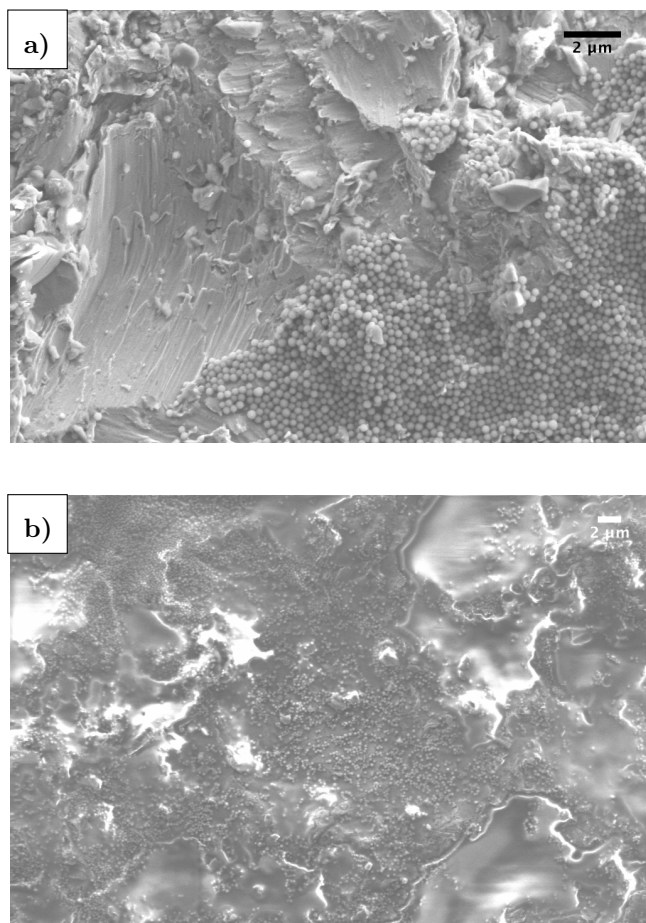


Figure 4.11: SEM images of surface structure obtained by one-step SC. a) The surface of F-Combo1. Areas covered by NPs, and areas without NPs are observed. b) The surface of F-Combo4 reveals thick, dense films of what was believed to be β -silane. The light areas appear due to charging.

4.4.4 Environmental Behavior

To further characterize the wetting behavior of the coatings, one of the most promising superhydrophobic surfaces was tested under different environmental conditions. Table 4.4 shows how the CA on F-SC3- β -DC developed when temperature and humidity was varied. A general trend of decreasing CA with decreasing temperature can be seen.

Table 4.4: CA as a function of temperature and humidity on F-SC3- β -DC.

Temperature [°C]	Humidity [%]	CA [°]
5.6	72.5	123
9.7	67.7	128
14.6	66.2	150
19.3	64.2	153
19.5	46.5	156
24.8	39.6	154
24.8	60.0	157

To further visualize the trend achieved at 60-70% humidity, the CA was plotted as a function of temperature, as shown in Figure 4.12. The plot shows a relatively stable CA down to about 15°C, and then a sharp decrease down to 10°C.

When the chamber was closed and the temperature lowered without humidity control, the humidity was found to stay relatively constant. In a preliminary experiment the humidity was 67% at 19°C. After being cooled down to 5°C in the course of 5 minutes the humidity was 55%. After 5 more minutes at this temperature the humidity increase to 64%, and after 10 minutes it was 67%.

Figure 4.13 shows how the CA of a droplet deposited at room temperature changed when the temperature was decreased on four different samples; F-SC3- β -DC, F-SC3- β -5S-DC, C1-SC3- β -DC, and F-Combo4. The temperature was lowered by about 1°C/min, and the CA was recorded every minute. The droplets stayed liquid even below 0°C, and the plots stop at the temperature where the droplets froze. The plots follow a similar trend to that of Figure 4.12.

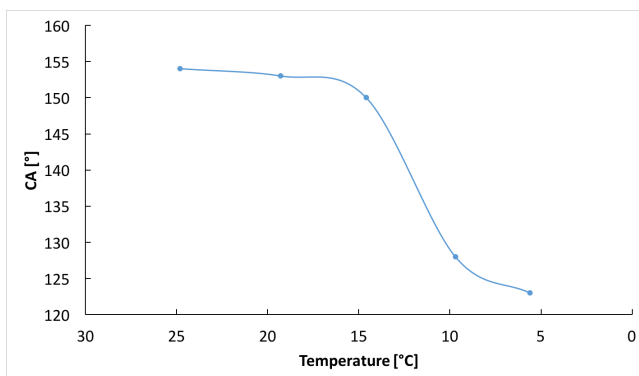


Figure 4.12: CA development as a function of temperature on sample F-SC3- β -DC. The humidity was controlled at a level in the 60-70% range, and the exact values for each data point can be found in Table 4.4.

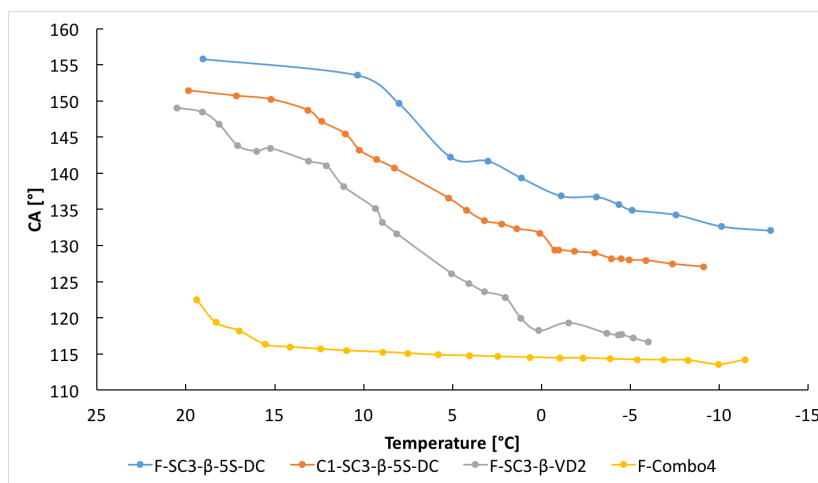


Figure 4.13: Development of CA as a the temperature was decreased approximately $1^{\circ}\text{C}/\text{min}$ on four different samples; F-SC3- β -DC, F-SC3- β -5S-DC, C1-SC3- β -DC, and F-Combo4. The CA of a $8\ \mu\text{L}$ droplet was measured until the droplet froze.

4.5 Icing Characteristics

In the following section the icing characteristics, in terms of the barrier against ice formation, delay of ice formation at a given temperature and cyclic icing behavior, of the coatings made in this work will be presented.

4.5.1 Barrier for Ice formation

The results for the barrier against ice formation are summed up in Table 4.5. The CA at deposition at chamber temperature of 5°C is included as well, which was below the superhydrophobic requirement of 150° for all samples.

In icing barrier experiments the droplets froze by the same mechanism, characterized by a sudden change in transparency and then a volume increase. The image series shown in Figure 4.14 shows an example of a typical icing process. The time after the first image was taken is indicated in the top left corner of each image. In Figure 4.14 a) the droplet was still liquid, and in b) 0.527 seconds later the ice formation started with the droplet turning black. In reality the droplet turned opaque, but appeared black on camera due to reflection or reduced transmission. In Figure 4.14 c) to e) the volume increased. The droplet was considered to be completely frozen when a pointy tip formed, as shown in Figure 4.14 f). After such a tip had formed no further volume increase was observed.

4.5.2 Cyclic Behavior

F-SC3- β -5S-DC, which showed the highest barrier against ice formation, and C1-SC3- β -5S-DC and F-SC3- β -VD2 that both showed quite low barriers, were put through three cycles of icing and de-icing. Table 4.6 shows the temperature required for the droplet to freeze, and the CA achieved, at 5°C, when the droplet was thawed after each freezing. Cycle 0 refers to the starting point before the first cycle.

The CA was also measured during cooling. Figure 4.15 shows how the CA developed during the three cooling stages. Figure 4.15 a) show the development for sample F-SC3- β -5S-DC and b) for sample F-SC3- β -VD2. CA_1 refers to the first cooling, CA_2 to the second and CA_3 to the third.

Table 4.5: Temperature required for formation of ice on the different samples. The droplet was deposited at chamber temperature of 5°C and the CA was measured. Then the temperature was gradually lowered until the droplet froze and the freezing temperature was noted. Most of the samples were only tested once ⁽¹⁾, however some samples were put through a second experiment ⁽²⁾. The droplet size was 8 μ L.

Sample ID	CA ¹ _{start} [°]	Icing Temperature ¹ [°C]	Icing Temperature ² [°C]
F	61	-5.3	
C	82	-4.6	
C1	83	-1.5	
F- β	123	-9.2	
C- β	124	-1.3	
C-SC1- β -DC	124	-12.3	
F-SC2- β -DC	132	-12.3	
C-SC2- β -DC	131	-9.0	
C-SC3- β -SC3	124	-6.1	
F-SC3- β -SC3	126	-9.5	
F-SC3- β -DC	126	-12.3	-10.8
F-SC3- β -VD2	113	-2.2	-5.6
F-SC3- β -5S-DC	126	-14.8	-13.4
C1-SC3- β -5S-DC	129	-2.3	-5.6
F-SC3- β -VD3	99	-9.1	
C1-SC3- β -VD4	115	-4.9	
F-SC3- β -SC2	114	-7.5	
F-DC- β -SC1	124	-9.9	
F-DC- β -VD3	94	-3.5	
F-SPC1- β -DC	135	-9.8	
F-SPC2- β -DC	124	-6.0	
F-Combo1	125	-12.5	
F-Combo2	120	-11.6	
F-Combo3	119	-10.1	
F-Combo4	119	-11.9	-12.9

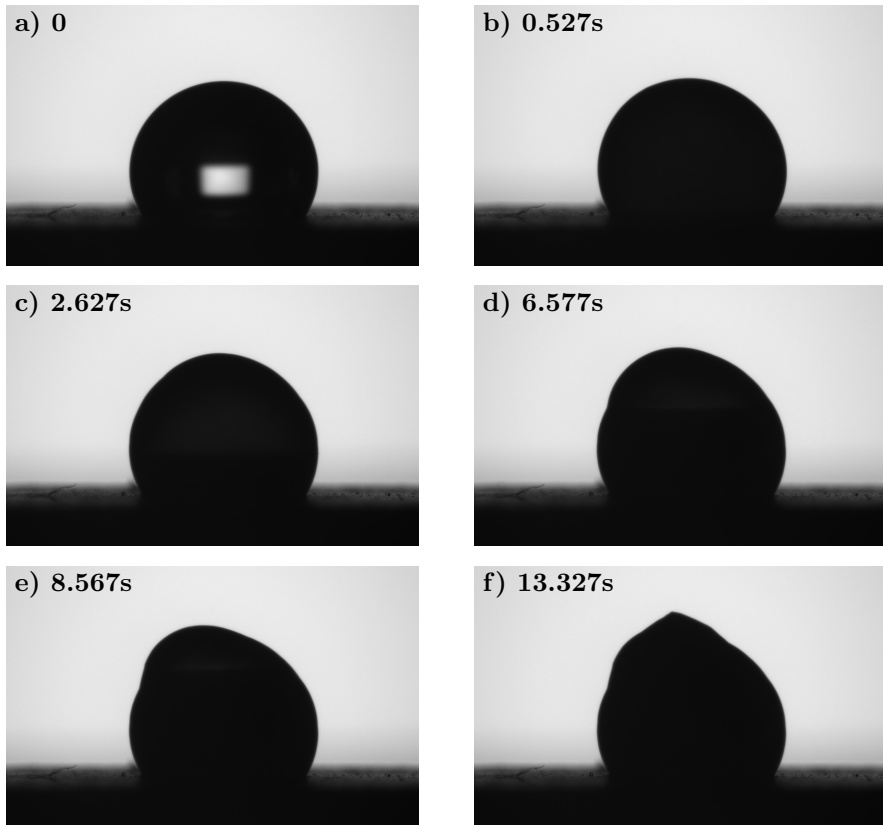


Figure 4.14: Mechanism of freezing on sample F-SC- β -5S-DC. The time after the first image was taken is indicated in the top left corner. The recorded temperature was -14.8°C . a) The droplet was still liquid, and b) the freezing started with the droplet becoming black. c) To e) the volume increased, causing the droplet to deform. f) The droplet was considered to be frozen solid.

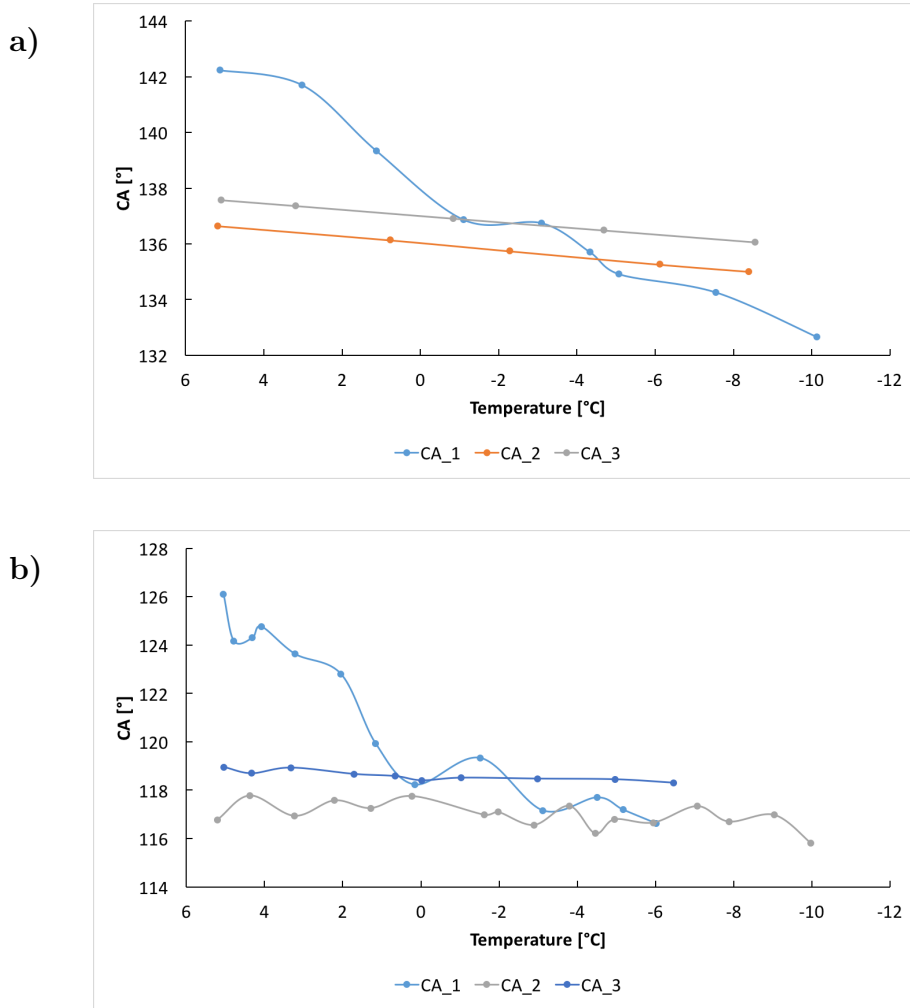


Figure 4.15: CA development during cooling in icing/de-icing cycles. a) Sample F-SC3- β -5S-DC and b) sample F-SC3- β -VD2. CA_1 refers to the first cooling, CA_2 to the second and CA_3 to the third.

Table 4.6: Temperature required for ice formation as a function of cycles and CAs achieved before and after freezing. Cycle 0 refers to the starting point before the first freezing.

Sample ID	Cycle	Freezing Temperature [°C]	CA [°] at 5°C
F-SC3- β -5S-DC	0	-	142
	1	-13.2	137
	2	-9.9	138
	3	-11.7	140
C1-SC3- β -5S-DC	0	-	135
	1	-9.5	130
	2	-10.0	132
	3	-7.5	130
F-SC3- β -VD2	0	-	126
	1	-6.5	118
	2	-10.5	119
	3	-7.4	119

Wetting Hysteresis

The CA was also measured after a droplet had been frozen and the substrate was heated back up again. Figure 4.16 shows the wetting hysteresis obtained on C1-SC3- β -5S-DC and F-Combo4. The software did not have the ability to measure the CA of the frozen droplet, but it did not change noticeably during heating before the droplet melted around 5°C.

Stability Over Time

To quantify how much of the change in CA during cooling was an effect of time, and not temperature, the CA on F-Combo4, F-SC3- β -VD2, F-SC3- β -DC, and F-SC3- β -5S-DC was measured every minute for 14 minutes while keeping the temperature constant at 20°C. The development in CA for the samples is shown in Figure 4.17.

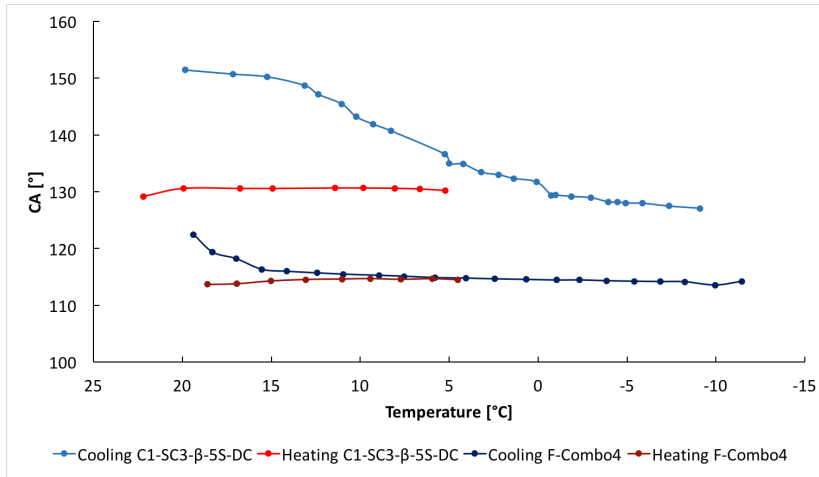


Figure 4.16: Wetting hysteresis on samples C1-SC3-β-5S-DC and F-Combo4. 8 μL droplets were deposited at 20°C and cooled down with 1 °C/minute until they froze, and then heated at the same rate back to 20°C.

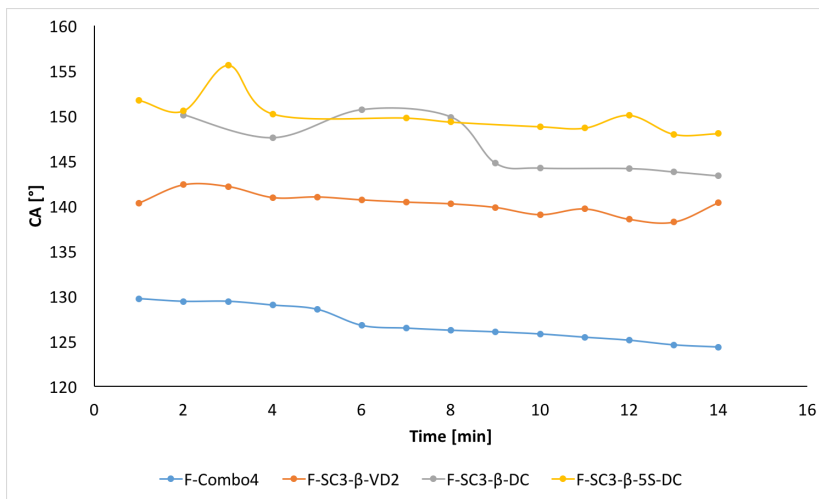


Figure 4.17: CA development of 8 μL droplet over time at a constant temperature of 20°C.

4.5.3 Delay of Ice Formation

Table 4.7 shows the time it took before a 8 μL droplet froze when deposited at -10°C . If the droplet started freezing on impact, the delay of ice formation was set to zero. 1 hour was set as the maximum limit for measuring freezing delay. Sample F-SC3- β -DC was tested twice, and Figure 4.18 shows how the icing occurred in the first experiment. In Figure 4.18 a) the liquid droplet just before ice formation can be seen, in b) the ice crystal on the right in the image came into contact with the droplet and it immediately turned black. In Figure 4.18 c) further ice formation was indicated by an increase in volume, and in d) the droplet was frozen solid indicated by the pointy tip.

Table 4.7: Delay of ice formation at -10°C . The delay on F-SC3- β -DC was measured twice, as indicated by F-SC3- β -DC². The droplet size was 8 μL .

Sample ID	CA [°] at -10°C	Temperature [°C]	Delay of Ice Formation [min]
F-SC3- β -DC	124	-10.0	13
F-SC3- β -DC ²	119	-10.2	>60
F-SC3- β -VD2	N/A	-10.3	0
F-SC2- β -DC	118	-10.2	>60
F-SC3- β -5S-DC	106	-10.3	30
C1-SC3- β -5S-DC	126	-10.2	5
F-Combo4	N/A	-10.0	0

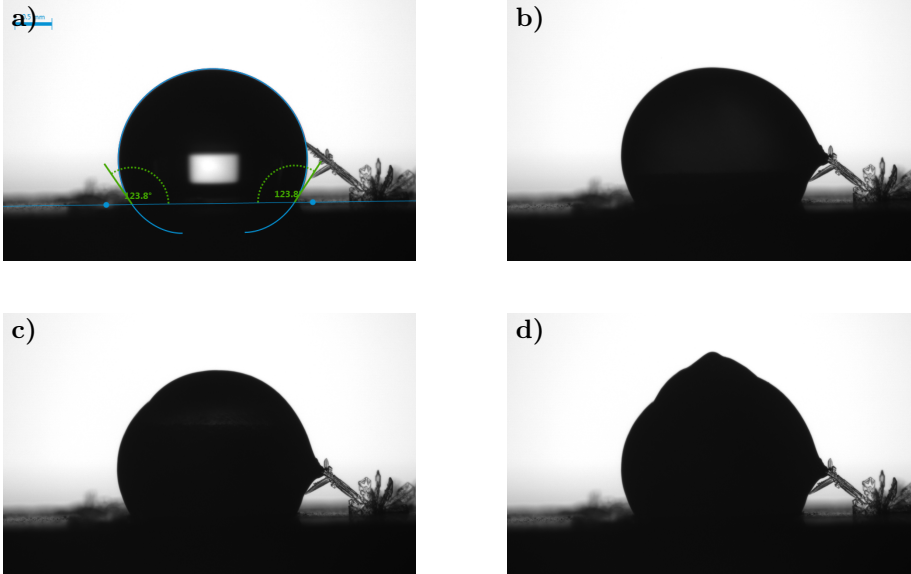


Figure 4.18: Mechanism of freezing on sample F-SC3- β -DC, first experiment. a) The liquid droplet just before freezing started, b) the first sign of ice formation as the droplet turned black, c) further freezing indicated by increase in volume, and d) the droplet was frozen solid indicated by the pointy top.

For the droplets which froze immediately after coming in contact with the samples, F-SC3- β -VD2 and F-Combo4, it was observed that the freezing started from the substrate. Figure 4.19 shows snapshots of the freezing of a droplet on sample F-Combo4. The time after deposition is indicated in the top left corner. The apparent high CA in Figure 4.19 a) can be attributed to the droplet freezing immediately after coming into contact with the surface. In the course of 36 seconds the ice phase gradually moved upward in the droplet, as shown in Figure 4.19 b) to e), and the ice formation was also evident from the volume of the droplet increasing. In Figure 4.19 f) the droplet was frozen solid.

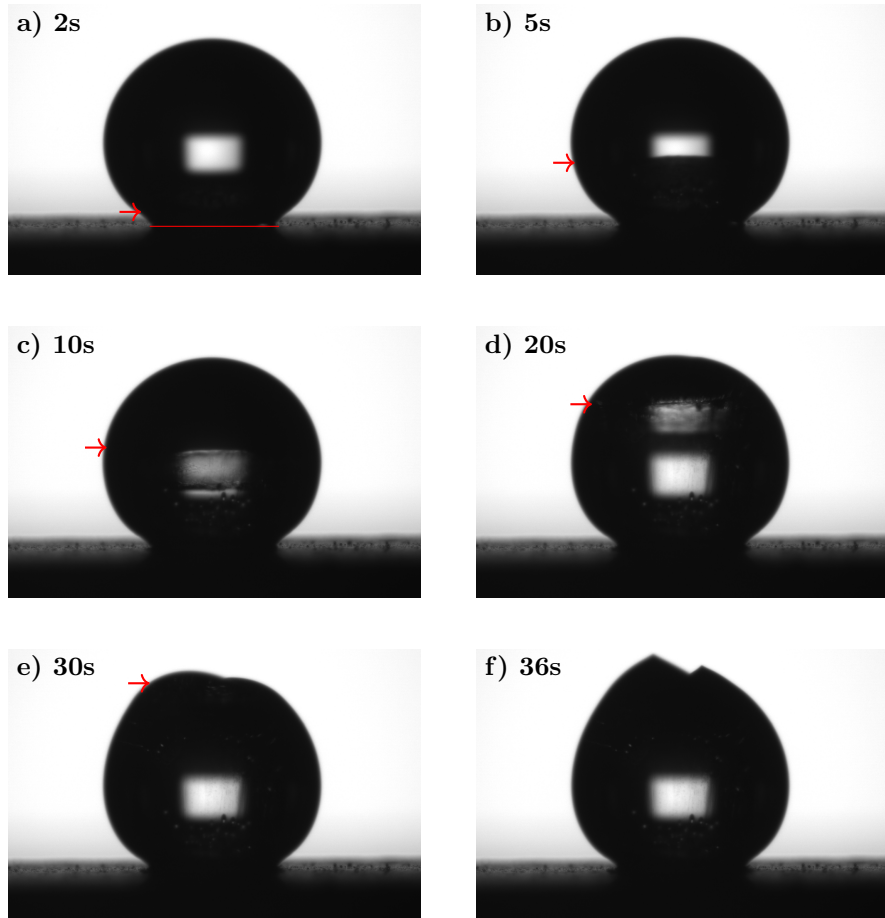


Figure 4.19: Mechanism of freezing on sample F-Combo4. The arrow marks the position of the ice front in each image, and in a) the interface between droplet and surface is marked by a red line. a) An apparently high CA appeared as the droplets started to freeze when it came into contact with the substrate. b) - e) The ice front moved upwards, before the droplet was frozen solid in f). The time in the top left corner indicates the time after deposition.

Chapter 5

Discussion

5.1 Surface Structure

Variations in the surface structures was influenced by the method for introducing microroughness, as well as the method used for deposition of nanoparticles (NPs). Advantages and disadvantages of the methods used are therefore of great importance.

5.1.1 Microroughness

As expected sandblasting (SB) with smaller sand grains yielded a lower average roughness on the steel surfaces. Larger particles will induce more damage on the surface when blasted with the same pressure and distance from substrates. Not only did the smaller sand grains produce a finer structure, the variation across the surfaces was also smaller. At coarse (C) surfaces a standard deviation of up to 28% was observed, whereas the fine (F) surfaces only deviated with about 12%. There was also a larger difference between two batches for the C sand. There can be many explanations for this. The C sand had a wider size distribution, causing larger variation between and on one sample. By sieving the F sand it was found to be in the size range 140 to 200 μm , whereas the grains in the C sand were reported to be between 500 and 1000 μm . Secondly, the first C batch was SB by used sand, whereas for the second batch the SB was

performed using fresh sand. The used sand might have decreased in size due to wear.

5.1.2 Size of Nanoparticles

The protocol for producing NPs was adopted from earlier work by Raymond Luneng [1], who reported the particles to have a mean size of 221 nm with a standard deviation of 8 nm. In this work the particles were found to be 261 ± 21 nm. The difference in reported size is mainly thought to come from the method used. Luneng deposited the particles on TEM-grids and imaged then using a scanning-transmission electron microscope (S(T)EM) in the transmission mode. The area of each particle was used for calculating the diameter. In this work a single image taken by the SEM was analyzed with ImageJ. Factors inducing uncertainty include the rough surface inducing height variation in the image leading some particles being closer to the detector than others, and that the exact outline of each particle was difficult to determine. In all images taken the particles appeared to be uniform in size. Luneng's method is considered to be more accurate and therefore the size reported by Luneng is believed to be more correct. However, this should be confirmed by a second measurement with S(T)EM.

5.1.3 Coating Method

Spray coating (SC) was considered the most promising method for deposition of NPs as the method is scalable, and has potential for very uniform and reproducible coverage. The contact angle (CA) measurements also showed that SC gave the best surfaces in terms of low roll-off angles (ROAs). The method provided good control over the amount deposited, as seen in Figure 4.5 and Figure 4.6, and the speed of the tip and distance between lines could have been adjusted for even better results. One challenge with this method is the stability of the particle sol and the creation of larger aggregates over time. Such an aggregate was found on one of the samples, shown in Figure 5.1.

In order to stop aggregates from forming, and to slow down sedimentation, the syringe was subjected to ultrasound. The sol would still pass through long tubings without any mixing. A cleaning step before each spraying was therefore

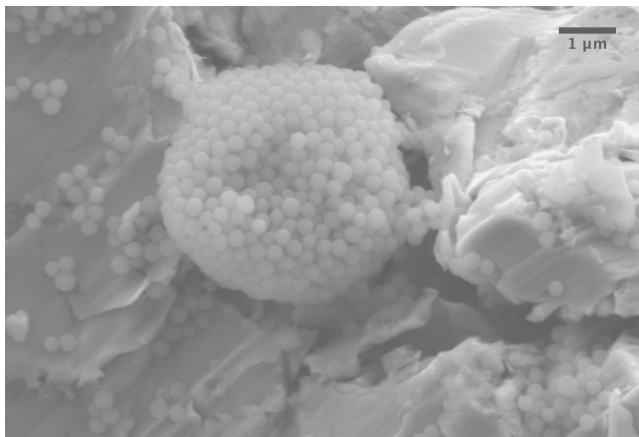


Figure 5.1: Aggregate of particles found on an SC sample.

applied. After these measures were taken no such aggregates were found, and the particle sol was found to be sufficiently stable.

Earlier work by the author and others on dip coating (DC) found a problem with lines forming and variable results [1, 3]. In addition, the results from DC was found to depend significantly on the cleaning method used. In this work, however, only one cleaning method was used and the coverage still varied. The thickness of the lines formed by DC in this work was attempted quantified, as seen in Figure 4.4. The result showed that the aggregates can become so thick that they completely cover the underlying microstructure, yielding a purely nanostructured surface instead of the desired hierarchical structure.

Spin coating (SPC) is another possible method for deposition of NPs, but like DC it is hard to scale up. Other predicted problems of the method was non-uniform coverage and irregularities due to the underlying microstructure. Therefore the method was not given much attention, and only two different speeds were tested. As described by Equation 2.11 the thickness decreased when the spin speed increased. Though the method produced thicker nanoparticle coverage towards the edges of the samples, it worked reasonably well. During SPC the sol is gradually drawn outwards by the centrifugal force (see Section 2.4.3), and so if the spin-off time is too short more sol will be collected at the edges of the sample. In addition the roughness of the substrate may hinder the spin-off

of sol. The method could be further optimized with regards to spin-up acceleration, spin-off speed and spin-off time, though irregularities due to the rough surface still will be present. Based on the current results the spin speed should be kept lower than 800 rpm, the spin time should be increased, and a low acceleration also seems sensible. A low speed will render dense coverage, whereas a longer spin time may decrease the observed edge effects.

Figure 5.2 illustrates the surface structures obtained by different amounts of NPs deposited. In Figure 5.2 a) NPs are spread out on the surface, yielding a nanoroughness on the scale of the particles. When the particles are closer together, as achieved by SC with 1.0 mL/min and illustrated in Figure 5.2 b), the nanoroughness becomes smaller than the particle size. A dense coverage was found to yield low ROAs and CAHs, and thus the structure shown in Figure 5.2 b) is preferred. However, a too thick NP layer will cover the underlying microstructure, as seen for DC samples, yielding higher ROAs.



Figure 5.2: Illustration of surface structures obtained by deposition of different amounts of NPs. a) NPs spread out on the surface and b) NPs deposited in an even layer. The nanoroughness shown in a) is larger than that in b). The microroughness of the underlying substrate is identical in the two illustrations.

5.2 Assessment of CA Measurements

The value of measured CAs, ROAs and contact angle hysteresis (CAHs) varied. Some of this was believed to come from non-uniformity in the coatings, both in terms of structure and β -silane coverage. Also, the method used might have induced some errors.

5.2.1 Surface Structure vs Surface Chemistry

As demonstrated by this work a hierarchical structure is necessary to meet both requirements of a superhydrophobic surface, with a CA above 150° and a CAH or ROA lower than 10° . A good coverage of β -silane was also necessary to render the surfaces superhydrophobic. Vapor deposition (VD) was generally not found to give CAs larger than 150° , though higher CAs were achieved by the introduction of subsequent pumpings. In earlier work by the author [3], CAs larger than 150° were successfully achieved on steel surfaces where NPs were dip coated. One sample even showed a roll-off at an angle lower than 90° . In this work another instrument was used for measuring CAs, but the exact CA value is not important. In addition, hydrochloric acid was used for cleaning the substrates in earlier work, which might have rendered the surface more reactive than the cleaning with isopropanol in this work. Another factor of importance for β -silane coverage by VD was the amount of NPs present on the surface, as silanes have a much higher effectiveness in covering silica than steel [28]. The high ROAs observed on VD samples were believed to be due to the droplet being in a Wenzel or Petal state on the surface (see Section 2.1).

For SC of β -sol the ROAs achieved were generally higher than 10° , however the best results were achieved by DC. There may be several reasons for this. The β -sol was diluted prior to SC, in order to achieve a lower viscosity and to be able to fill the syringe without wasting too much β -silane, which is an expensive precursor. The amount of β -silane sprayed was based on the results of NP spraying, and as 0.5 mL/min was found to cover the surface without making it too wet (droplet/meniscus effects) this was considered a good starting point. The best results were achieved by a dilution of 1:1 with ethanol, but the ROAs were still higher than for DC. Further investigations should be made using even more layers, a non-diluted sol or an even more concentrated sol. The viscosity of the β -40S-sol was similar to that of the NP-sol (see Table 4.2), and not too high for spraying. Another reason for why DC gave better results may be that the silane molecules have more time to orientate (as described in Section 2.4.3), yielding a more favorable surface chemistry with more of the fluorinated chains pointing outwards. DC with the more concentrated β -5S-sol gave small improvements in both CA, ROA and icing temperature, suggesting that the surface chemistry is important.

Combined SC of NP-sol and β -40S-sol produced high CAs, but the ROAs were all above 90° . This may be attributed to the uneven NP coverage observed by

SEM (see Figure 4.11a). The surfaces had areas with almost no nanoroughness, increasing the probability of the droplets being in the Wenzel or Petal state. Also the coverage of β -sol may be uneven, further increasing the adhesion between droplet and surface. The F-Combo4 showed that too much sol will cover the underlying structure, so that a superhydrophobic state not can be achieved.

Coverage of β -silane

Though the CAs measured gave some indication about the β -silane coverage, it is hard to quantify due to the several factors involved. SEM images revealed some features believed to be broken pieces of β -silane film, or dense agglomerates, which were further characterized by using BSE mode, as shown in Figure 4.10. The two features marked by red rectangles, appear dark on the BSE image, suggesting that they indeed consist of other atoms than the underlying steel substrate. Other similar features on the surface, as well as the NPs, appeared dark in the BSE image. In BSE mode the contrast can be due to elemental contrast, or topographical contrast. The topographical contrast will lead to features rising from the surface appearing lighter. Such features would also appear lighter when detecting SE. The crack in the surface marked by a red arrow in Figure 4.10 marks an area that appears dark both in Figure 4.10 a) and b), showing how topographical contrast can be seen in BSE mode. There is no visible difference between the NPs and what is believed to be β -silane film on the surface, which is not surprising as both to a large extent (or completely) consist of silicon and oxygen.

Other methods for characterizing the coverage of β -silane were also considered, such as *energy-dispersive X-ray spectroscopy* (EDS) and *X-ray photoelectron spectroscopy* (XPS). EDS was tried on the FE-SEM used for imaging, but proved to be challenging. Probing of the surface demanded a low acceleration voltage of 5 keV, a large aperture of 300 μm and high current. Fluorine was considered the most relevant to look for, as silicon and oxygen would be present in the form of SiO_2 -NPs and carbon always being present due to atmospheric contamination. However, the characteristic X-ray energy of fluorine overlaps with the lowest characteristic energy of iron. The fluorine $\text{K}\alpha$ transition has an energy of 0.677 keV and the iron $\text{L}\alpha$ an energy on 0.705 keV [69]. The detector used had a maximum resolution of 0.123keV, and so the two (possibly different) peaks appeared as one large peak. In addition it should be mentioned that EDS even at low acceleration voltage will probe some of the bulk, further increasing signal

from iron. Also, the roughness of the surfaces provided challenges for the ZAF-correction¹ of the software, making it even harder to distinguish peaks from each other. However, the technique could be useful on other substrates, such as aluminum, where it should be applied on flat surfaces.

5.2.2 Sources of Error in CA and CAH Measurements

The standard deviation in the CAs, ROAs and CAHs measured should reflect the uniformity of the coating, but the method used could also have some inherent sources of error. The CA was measured by fitting the droplet and looking at the angle it formed with the surface. The fitting mode used, and the baseline set, were important factors for measuring CAs. Figure 5.3 a) shows a typical 8 μ L droplet on a coated surface, with the Young-Laplace fitting mode used for calculating the CA. When the same droplet, using the same baseline, was measured by the Tangent mode the result is the angles shown in Figure 5.3 b). This means that inherent in the Tangent mode is some difference between the right and left angle, possibly explaining why the CAHs measured consistently were higher than the ROAs. When the baseline was set higher, as in e) the measured CA was lower and when it was set lower, as in f), the CA as a consequence was measured to be higher. This indicates that the exact CA value is not that meaningful. In c) a droplet on a tilted surface can be seen, which is asymmetrical. When this droplet was fitted by the Young Laplace mode, as shown in c), the angles on each side appeared equal, but when the same droplet was fitted by the Tangent mode a CAH of 21.6° appears.

5.2.3 Environmental Behavior

The CA of the superhydrophobic (hierarchical) surfaces was found to greatly decrease when lowering the temperature and keeping the relative humidity relatively constant (see Figure 4.12 and 4.13). As the CAs were found to be stable when the droplets were kept at one temperature (see Figure 4.17), the effect was believed to be due to temperature changes. Other studies have shown similar effects when the surface has been gradually cooled down or been subject to sub-zero temperatures for some time [18, 70]. The change in CA was reported at temperatures below 15°C, and was attributed to water condensating on the

¹ZAF-correction is a abbreviation for atomic number (Z), absorption (A) and characteristic fluorescence (F) correction.

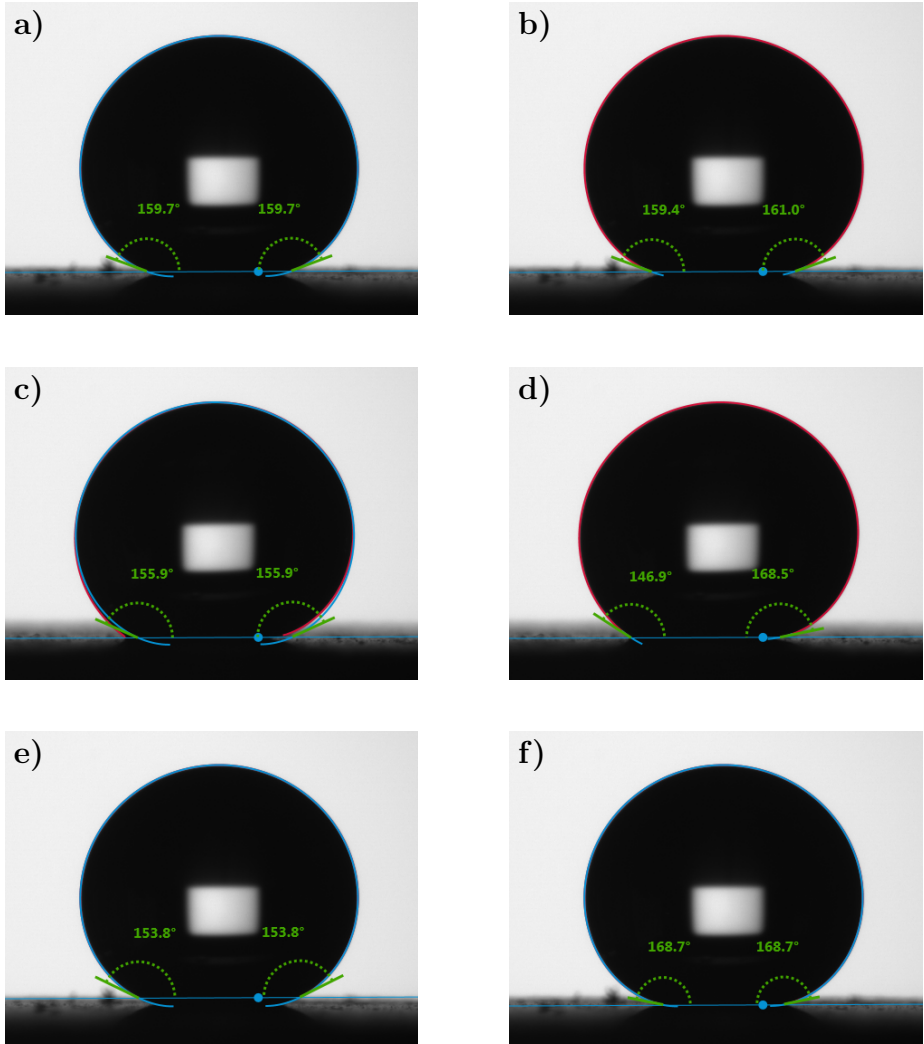


Figure 5.3: Importance of using the right baseline and fitting mode when measuring CA and CAH. a) Young Laplace on a symmetric droplet, and b) Tangent fitting mode on the same droplet. c) Young Laplace fitting of an asymmetric droplet during tilting, and d) Tangent fitting of the same droplet. e) And f) show the same droplet as in a) with the baseline set too high and too low, respectively.

surface. At subzero temperatures the same water will cause frost formation on the surface. In this work a drastic change in CA was observed in the 12 to 5°C range, suggesting that most of the water condenses around this temperature. Further decrease is seen after this point, but after one freezing the CA remained stable (see Figure 4.15), suggesting that the surface was completely covered by condensed water/frost. Figure 4.18 supports the hypothesis of water condensing on the surface, and later formation of ice, as clear ice crystals could be seen next to the droplet. The hypothesis was further substantiated by the fact that the CA of F-Combo4, a relatively flat surface as seen in Figure 4.11 b), did not decrease nearly as much as for the hierarchical surfaces.

In the cyclic experiments shown in Figure 4.15 the CA went back to approximately the same value as right before the droplet froze, suggesting that the surface indeed still was covered by condensed water. At this stage there might also have been some deterioration of the coating layer caused by the icing. The wetting hysteresis shown in Figure 4.16 show that the CA after freezing stays constant up to room temperature, and no water seemed to evaporate from the surface. The difference in CA before and after freezing was about 6° for F-Combo4 (at 18°C), and 21° for C1-SC3- β -5S-DC (at 20°C). The same effect has been found by others, with flat surface showing a much smaller wetting hysteresis than rough ones [70]. This suggests that the change in wetting state for rough surfaces was irreversible.

The Laplace equation gives the pressure difference across a curved interface [26]. Such curvatures are found on surfaces containing micro- and nanostructure. A higher vapor pressure will cause more water to condense, and so the rough surfaces are more affected than the flat. Smaller structures on the surface will have higher vapour pressures than larger features, which means a greater resistance against a Cassie-Baxter to Wenzel transition [71]. This explains why the structure illustrated in Figure 5.2 b) showed the lowest ROAs. Such surfaces thus have a lower threshold angle for the coexistence of both a Wenzel and Cassie-Baxter state, as explained by Equation 2.5.

5.3 Assessment of Icing Experiments

Ideally all icing experiments should be performed several times for each sample, utilizing different areas each time, as for the CA measurements. This would have given statistics on the variation on each surface, and trends on which surface

that was best would have been easier to observe.

The experiments for determining the barrier for ice formation revealed a large decrease in CA at 5°C compared to room temperature, and inspired the previously mentioned experiments under different environmental conditions. Another effect of the reduction in CA was the corresponding increase in contact area between the droplet and surface. The Cassie-Baxter state is a superhydrophobic state with air trapped in the structure, and the decrease in CA suggests that a change in the wetting state has occurred. Such a change has been reported by others, and is illustrated in Figure 5.4 [72].

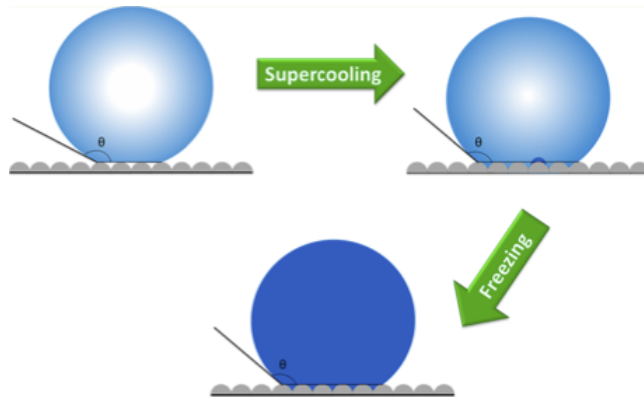


Figure 5.4: Change of wetting state under supercooling. Adapted from Heydari et al. [72].

The droplet was observed to freeze at higher temperatures on surfaces with C or C1 microstructure, than on those with F. This can be explained by the mentioned resistance for a wetting state transition being smaller for the coarser structures, meaning that the insulating air pockets are more easily removed. Others, as mentioned in Section 2.2.1, have shown similar effects with the probability for ice formation increasing with increasing particle size [20]. They attributed the effect to the free-energy barrier of nucleation on a the convex surface being greater on the smaller particles. Both the mentioned effects may have been of importance for the observations made in this work.

The barrier for icing on VD samples was observed to be lower than for DC, SC or Combo samples. This might not be that surprising as these samples also generally showed lower CA and high ROA (see Table 4.3), meaning a larger

contact area between droplet and surface. Surprisingly, F-Combo4, a sample showing both a relatively low CA and high CAH, had similar icing properties as the most hydrophobic samples. This suggests that size of features of the surface was more important than the reduced contact area. Also, the critical radius for ice nuclei is very small (5-10 nm) and it is in contact with only a small area of the surface, making the surface energy more important than the structure [72]. Also, this suggests that there is no direct correlation between superhydrophobic properties and icing properties.

As mentioned above the decrease in CA suggested a transition in wetting state, from Cassie-Baxter to Wenzel (or a petal effect), and when icing occurred the droplet was believed to be in complete contact with the surface. Others have attributed the anti-icing properties of superhydrophobic surfaces to the reduced heat transfer and interface area, as mentioned in Section 2.2.1, but the results here suggest that due to the change in wetting state these effects are minimal. The cyclic behaviors suggest that there was almost complete contact between the droplet and surface even for the first freezing, as no systematic decrease in anti-icing properties are found. After freezing, the samples were tilted by hand, and the droplet stuck to the sample at 90° for all cases, substantiating the hypothesis of a change in wetting state.

Others have also done similar measurements of icing characteristics [17, 72, 73]. However, direct comparison of their results to what was obtained here is difficult due to uncertainties and differences in humidity, droplet size, rate of cooling and whether it was the surface or air temperature that was reported.

Further experiments revealed that the temperatures obtained in the energy barrier experiments given in Table 4.5 included large uncertainties, as seen both for the samples tested twice and for the samples that were put through cyclic experiments. For C1-SC3- β -5S-DC the droplet froze at -2.3°C in the first experiment, and at -5.6°C in the second. In the cyclic experiments it froze at -9.5°C , -10.0°C and -7.5°C , giving a variation between the best and worst result of 7.7°C . F-SC3- β -VD2 also showed large variations, whereas F-SC3- β -DC, F-SC3- β -5S-DC and F-Combo4 showed more consistent results. This suggests that the fine samples with even β -silane coverage were more stable.

Some of the variations for C- and VD-samples can be explained by the ice nucleation being very dependent on the local environment. In two different experiments the droplet will naturally not be placed on the exact same area, and local variations will occur. Especially the C1 samples showed a large variance in roughness, varying from 4.1 to 6.9 μm . The coverage of β -silane on VD surface

was found to depend on NP coverage, making such surfaces more prone to large variations. When both structure and chemistry was more uniform, as achieved by a fine microstructure and DC of β -sol, the results were more stable. Others have observed similar spreads in freezing temperature, and attributed it to the stochastic nature of the nucleation process [41]. Further, the differences can be explained by the variation between the air and surface temperature, which will be elaborated in the next section.

5.3.1 Surface Temperature vs. Chamber Temperature

The temperature reported in all experiments was the temperature recorded by the temperature sensor inserted through the top of the chamber. A peltier element was controlled from a separate box, and adjusted the temperature from the bottom plate of the chamber. When the sensor was inserted, it was set in contact with the bottom plate, but it was also affected by the air in the chamber. The equipment did not offer a way of measuring only the surface temperature, and in the following discussion the set temperature and surface temperature will be assumed equal. The steel substrates were placed in direct contact with the bottom plate.

In experiments the focus was on making the recorded temperature follow a given rate. However, observations were made on the droplet freezing from the surface (see Figure 4.19) and large variations in freezing temperatures appeared. Thus, the surface temperature was thought to be more important. The thermal conductivity of air is 0.024 W/mK whereas steel is reported to conduct 16 W/mK, both at 25 °C [74]. Thus, it is likely that the surface temperature of the steel samples was lower than the general chamber temperature. In general the difference between the set temperature and recorded temperature was 5°C. Further investigations revealed that the recorded temperature followed a slope of 0.78 (see Figure A.1 in Appendix A.3), yielding a larger difference between the surface temperature and recorded temperature for more extreme temperatures. In Figure A.1 the orange line marks the ideal trend, with the set temperature and the recorded temperature being equal. The deviations between surface and recorded temperature can have been even larger than what is depicted here. Further complications apply for the delay of ice formation experiments, where the temperature had to be increased over time in order to keep a constant recorded temperature of -10°C.

The validity of all icing experiments would increase if the equipment offered a way to record the exact surface temperature. Other measures that could improve the results is to keep the substrates in the chamber longer before depositing the droplet, so that the difference between surface temperature and chamber temperature would be smaller. However, for the experiments where the temperature is gradually lowered this would not be possible, so a better solution might be to follow the exact same cooling program for the set temperature and rather let the recorded temperature deviate some. More measurements should be done on every sample to confirm the role of the surface temperature.

5.3.2 Icing Mechanism

Icing barrier experiments revealed that the first formation of ice was instantaneous, as the droplet became opaque. Further formation of ice took 10 to 15 seconds, where the ice front moved up from the surface and the volume increased. The droplet was considered to be completely frozen when a pointy tip formed on top of the droplet, and no further volume increase was observed after this point. Others have reported that the freezing of a water droplet on a surface can be divided into four steps; water cooling, rapid kinetic freezing, isothermal freezing, and ice cooling [75]. Several explanations have been made regarding what causes the droplet to turn opaque in the second step [44]. Some have attributed this to the release of air bubbles, as air is less soluble in ice than water, others claim that light scattering due to partially solidified water is the reason. The observations made in this work support the last explanation, which state that a solid ice shell forms around the droplet, still having a liquid center. In Figure 4.14 the droplet maintains a round shape after freezing, and the volume increase mostly occurs on top. This indicates that a solid shell has formed, and as the droplet freezes from the bottom and up the extra volume is pushed through the top part of the droplet.

During isothermal freezing the droplet is said to remain at the equilibrium freezing temperature of water, 0°C. The setup used in this work had no method for confirming the droplet temperature, but a freezing front moving up from the surface was observed. As the droplet solidifies the volume increased, finally resulting in a pointy top on the droplet. Since the droplet increased visually, it was believed that the droplet also increased in volume at the contact point between the droplet and surface, potentially destroying some of the coating structure.

At -10°C one can assume that the surface was wetted by condense/frost, based on the fact that the CA in the cyclic experiments was quite stable at such low temperatures. On the first delay experiment on F-SC3- β -DC this was further confirmed by a large ice crystal on the surface. This crystal grew into the droplet, and seemed to initiate icing. As described earlier, the barrier for ice formation is lower for heterogenous nucleation. The droplet froze immediately after coming into contact with the crystal, but in the second trial it did not freeze even after 60 minutes, substantiating the hypothesis of the ice crystal inducing freezing.

During measurements of delay of ice formation a slightly different freezing mechanism was observed for the droplets freezing upon contact, as seen in Figure 4.19. Here, no sudden change in transparency of the droplet can be seen, which can be explained by the fact that the droplet did not have time to become super-cooled. Instead, the droplet went directly to step three of freezing, with an ice front moving upwards. If the droplet froze after some time in the icing delay experiments the same mechanism as for icing barrier experiments was observed. Thus, we have two possible mechanisms in icing delay experiments determined by the properties of the surface.

5.3.3 Ice Adhesion Strength

Ice adhesion has not been measured in this work. However, some predictions can be given based on the CA_{rec} measured. Ice adhesion strength is found to correlate with the water adhesion strength given in Equation 2.8 [46]. F-SC3- β -5S-DC, the sample that showed the highest barrier against ice formation, also had the highest CA_{rec} of $147 \pm 1^{\circ}$. Other superhydrophobic samples showed a CA_{rec} around 135° , whereas the worst sample was F-Combo1 with a CA_{rec} of $93 \pm 3^{\circ}$. The $(1 + \cos \theta_{rec})$ in Equation 2.8 term equals about 0.16 when CA_{rec} is 147° , 0.29 when CA_{rec} is 135° and 0.95 when CA_{rec} is 93° . Thus, the difference in ice adhesion strength between the samples can be sixfold. However, all samples showed ROAs larger than 90° after freezing, and a corresponding, low CA_{rec} . Thus, the difference between samples might not be as large as a depicted here.

Chapter 6

Conclusion

The superhydrophobic properties of the surfaces studied in this work were found to depend both on surface structure and surface chemistry. The magnitude of the microstructure did not greatly affect the obtained contact angles (CAs) and roll-off angles (ROAs). A dense coverage of nanoparticles (NPs) was found necessary for achieving low ROAs, but high CAs was also found on surfaces without NPs. The best method for depositing NPs was spray coating. The nanoroughness obtained was most even and uniform, it produced the samples showing the lowest ROAs, and lastly, it is the most relevant method to use when coating larger structures. A dense, even coverage of NPs may also be beneficial as it increases the resistance against a Cassie-Baxter to Wenzel transition. When this was combined with dip coating of the hydrophobic top coating based on 1H,1H,2H,2H-perfluorooctyltriethoxysilane (β -silane), the best superhydrophobic surface, in terms of low ROA, was achieved. This surface showed CA of $158 \pm 2^\circ$, ROA of $8 \pm 2^\circ$ and contact angle hysteresis (CAH) of $19 \pm 3^\circ$.

The CAs on the investigated surfaces greatly decreased when the temperature was lowered, and the decrease was more prominent for rough surfaces. The decrease was believed to be due to an irreversible transition in wetting state from the favorable Cassie-Baxter to the immobile Wenzel state induced by water condensing on the surfaces. When heating a droplet after freezing, the CA did not increase back to initial values, inducing a wetting hysteresis on the surface.

The mentioned best superhydrophobic sample did show the highest barrier against ice formation, with a freezing temperature of -14.8°C . However, when a droplet was deposited at -10°C on this surface it froze after 30 minutes. Other samples showed freezing delays surpassing 1 hour. During 3 cycles of icing and de-icing no trend of decreasing anti-icing properties was found. In addition, a flatter surface showing a CA of only $121\pm 1^{\circ}$ had similar icing properties as the hierarchical surfaces. Hence, no definite correlation between superhydrophobicity and anti-icing properties was found.

The icing experiments revealed large deviations in freezing temperature between experiments, with the largest deviation being 7.7°C . This was found on a surface sandblasted with coarse sand, where NPs were deposited by spray coating and β -silane by dip coating. The deviations can be explained by non-uniformities in the surface structure, uneven coating and uncertainty around the exact surface temperature during experiments. Further experiments are needed to conclude which surface showed the best anti-icing properties, but some trends are suggested. The microroughness seems to be important, with higher roughness being less favorable due to a smaller barrier against the Cassie-Baxter to Wenzel transition. However, the need of microstructure is questioned. The surface chemistry is important both for icing and for stability of the wetting state, so an even coverage of β -silane is necessary.

Chapter 7

Further work

Anti-icing surfaces is a complex field, and this thesis substantiates that more work is necessary. The superhydrophobic properties of the surfaces in this work can be improved by further optimization of both surface structure and chemistry. For nanoparticles the spray coating technique should be optimized in terms of nozzle speed and distance between spraying lines. Deposition of smaller particles should be tested, to obtain an even smoother nanostructure. The deposition of β -silane by spray coating should also be further investigated, by using non-diluted sol. For the combined spraying of both particles and silane, functionalization of the particles should be studied. As the superhydrophobic properties deteriorate when the surfaces are cooled down, the focus should be on producing more stable surfaces.

As no direct correlation between hydrophobic properties and anti-icing abilities were found in this work, or by others, the focus for anti-icing surfaces should shift into making the surfaces with the best anti-icing properties. The need of nano- and microstructure should be questioned, and if needed, minimized. Other improvements include the incorporation of a liquid lubricating layer in the structure. Surfaces should be more targeted for a specific application, as the properties vary with environmental conditions. Also, the possibility of combining the surfaces with other de-icing techniques should be looked into. Further testing of the durability and mechanical properties is necessary, as well as measuring the ice adhesion.

To further substantiate the trends observed in this work, each sample should be tested several times. By doing this the exact effect of coating parameters, rather than uncertainties due to non-uniformity and surface temperature, can be investigated. As the droplets are found to freeze from the surface up, the focus should be on measuring the surface temperature and not the temperature of the surrounding air.

Bibliography

- [1] Raymond Luneng. Development of hydrophobic surfaces for anti-icing applications. Masters thesis, Department of Materials Science and Engineering, NTNU, 2015.
- [2] Ole-Bjørn Ellingsen Moe. Development of hydrophobic surfaces for anti-icing applications. Master thesis, Department of Materials Science and Engineering, NTNU, 2015.
- [3] Hanna Sandvoll Vassmyr. Development of hydrophobic surfaces for anti-icing applications. Spezialization project, Department of Materials Science and Engineering, NTNU, 2015.
- [4] Effluent limitation guidelines and new source performance standards for the airport deicing category. United States Environmental Protection Agency, 2012.
- [5] De-icing wind turbines. <http://www.engineering.com/ElectronicsDesign/ElectronicsDesignArticles/ArticleID/6776/De-Icing-Wind-Turbines.aspx>. Last accessed May 30th 2016.
- [6] M. J. Kreder, J. Alvarenga, P. Kim, and J. Aizenberg. Design of anti-icing surfaces: smooth, textured or slippery? *Nature Reviews Materials*, 1(1):15003, 2016.
- [7] Charles C. Ryerson. Ice protection of offshore platforms. *Cold Regions Science and Technology*, 65(1):97–110, 2011.
- [8] Frigid weather heightens ice hazards. <http://www.riskmanagementmonitor.com/frigid-weather-heightens-ice-hazards/>. Last accessed May 31st 2016.

- [9] Oil exports begin from gazprom's gulf of ob field. <http://www.offshoreenergytoday.com/oil-exports-begin-from-gazproms-gulf-of-ob-field/>. Last accessed May 31st 2016.
- [10] Teknisk ukeblad: Her spyer helikopteret bort et tykt lag med is. <http://www.tu.no/kraft/2015/02/01/her-spyler-helikopteret-bort-et-tykt-lag-med-is>. Last accessed May 30th 2016.
- [11] Thermon, arctic offshore and maritime heating solutions. <http://www.thermon.com/us/arctic.aspx>. Last accessed May 30th 2016.
- [12] S. A. Kulinich and M. Farzaneh. How Wetting Hysteresis Influences Ice Adhesion Strength on Superhydrophobic Surfaces. *Langmuir*, 25(16):8854–8856, 2009.
- [13] S. Jung, M. Dorrestijn, D. Raps, A. Das, C. M. Megaridis, and D. Poulikakos. Are Superhydrophobic Surfaces Best for Icephobicity? *Langmuir*, 27:3059–3066, 2011.
- [14] L. B. Boinovich, A. M. Emelyanenko, V. K. Ivanov, and A. S. Pashinin. Durable icephobic coating for stainless steel. *ACS Applied Materials and Interfaces*, 5(7):2549–2554, 2013.
- [15] J. B. Boreyko and C. P. Collier. Delayed frost growth on jumping-drop superhydrophobic surfaces. *ACS Nano*, 7(2):1618–1627, 2013.
- [16] Z. Yuan, M. Wang, J. Huang, X. Wang, J. Bin, C. Peng, S. Xing, J. Xiao, J. Zeng, X. Xiao, X. Fu, H. Gong, D. Zhao, and H. Chen. Icephobicity and the effect of water condensation on the superhydrophobic low-density polyethylene surface. *Surface Topography: Metrology and Properties*, 3(2):25001, 2015.
- [17] A. Alizadeh, M. Yamada, R. Li, W. Shang, S. Otta, S. Zhong, L. Ge, A. Dhinojwala, K. R. Conway, V. Bahadur, A. J. Vinciguerra, B. Stephens, and M. L. Blohm. Dynamics of Ice Nucleation on Water Repellent Surfaces. *Langmuir*, 28:3180–3186, 2012.
- [18] S. A. Kulinich, S. Farhadi, K. Nose, and X. W. Du. Superhydrophobic Surfaces: Are They Really Ice-Repellent? *Langmuir*, 27(1):25–29, 2011.

- [19] G. Momen, R. Jafari, and M. Farzaneh. Ice repellency behaviour of superhydrophobic surfaces: Effects of atmospheric icing conditions and surface roughness. *Applied Surface Science*, 349:211–218, 2015.
- [20] L. Cao, A. Jones, V. K. Sikka, J. Wu, and D. Gao. Anti-Icing superhydrophobic coatings. *Langmuir*, 25(21):12444–12448, 2009.
- [21] Ellen-Kristin Raasok. Hydrophobic coatings for anti-icing applications. Master thesis, Department of Materials Science and Engineering, NTNU, 2014.
- [22] Aase Marie Halvorsen. Hydrophobic coatings for anti-icing applications. Master thesis, Department of Materials Science and Engineering, NTNU, 2014.
- [23] Vegard Hornnes. Development of hydrophobic surfaces for anti-icing applications. Spezialisierung project, Department of Materials Science and Engineering, NTNU, 2015.
- [24] N. R. Baddoo. Stainless steel in construction: A review of research, applications, challenges and opportunities. *Journal of Constructional Steel Research*, 64(11):1199–1206, 2008.
- [25] T. Young. An Essay on the Cohesion of Fluids. *Philosophical Transactions of the Royal Society of London*, 95(0):65–87, 1805.
- [26] Paul C. Hiemenz and Raj Rajagopalan. *Principles of Colloid and Surface Chemistry*. Taylor and Francis, third edition, 1997.
- [27] Abraham Marmur. The Lotus Effect: Superhydrophobicity and Metastability. *Langmuir*, (20):3517–3519, 2004.
- [28] Barry Arkles. Hydrophobicity, hydrophilicity and silane surface modification version 2.0. http://www.gelest.com/themencode-pdf-viewer/?file=http://www.gelest.com/wp-content/uploads/Goods-PDF-brochures-Hydrophobicity_Catalog.pdf. Handbook from Gelest Inc. Last accessed June 12th 2016.
- [29] Robert N. Wenzel. Resistance of Solid Surfaces. *Ind. Eng. Chem.*, 28:988–994, 1936.
- [30] A.B.D. Cassie and C Baxter. Wettability of porous surfaces,. (5):546–551, 1944.

- [31] C. Antonini, M. Innocenti, T. Horn, M. Marengo, and A. Amirfazli. Understanding the effect of superhydrophobic coatings on energy reduction in anti-icing systems. *Cold Regions Science and Technology*, 67(1-2):58–67, 2011.
- [32] A. Lafuma and D. Quéré. Superhydrophobic states. *Nature materials*, 2(7):457–60, 2003.
- [33] H. Liu, X. Wang, and H. Ji. Fabrication of lotus-leaf-like superhydrophobic surfaces via Ni-based nano-composite electro-brush plating. *Applied Surface Science*, 288:341–348, 2014.
- [34] Z. Chu and S. Seeger. Superamphiphobic surfaces. *Chemical Society reviews*, 43:2784–98, 2014.
- [35] W. Barthlott and C. Neinhuis. Purity of the sacred lotus, or escape from contamination in biological surfaces. *Planta*, 202:1–8, 1997.
- [36] L. Feng, Y. Zhang, J. Xi, Y. Zhu, N. Wang, F. Xia, and L. Jiang. Petal Effect: A Superhydrophobic State with High Adhesive Force. *Langmuir*, 24(8):4114–4119, 2008.
- [37] J. Chen, Z. Luo, Q. Fan, J. Lv, and J. Wang. Anti-Ice coating inspired by ice skating. *Small*, 10(22):4693–4699, 2014.
- [38] P. Kim, T. Wong, J. Alvarenga, M. J. Kreder, W. E. Adorno-Martinez, J. Aizenberg, and K. Al. Liquid-Infused Nanostructured Surfaces with Extreme Anti-Ice and Anti-Frost Performance. *ACS Nano*, 6(8):6569–6577, 2012.
- [39] S. B. Subramanyam, K. Rykaczewski, and K. K. Varanasi. Ice adhesion on lubricant-impregnated textured surfaces. *Langmuir*, 29(44):13414–13418, 2013.
- [40] Q. Liu, Y. Yang, M. Huang, Y. Zhou, Y. Liu, and X. Liang. Durability of a lubricant-infused Electrospray Silicon Rubber surface as an anti-icing coating. *Applied Surface Science*, 346:68–76, 2015.
- [41] V. Hejazi, K. Sobolev, and M. Nosonovsky. From superhydrophobicity to icephobicity: forces and interaction analysis. *Scientific reports*, 3:2194, 2013.
- [42] A. M. Boinovich and L. B. Emelyanenko. Anti-icing potential of superhydrophobic coatings. *Mendeleev Communications*, 23:74–75, 2013.

- [43] H. Wang, G. He, and Q. Tian. Effects of nano-fluorocarbon coating on icing. *Applied Surface Science*, 258(18):7219–7224, 2012.
- [44] L. Oberli, D. Caruso, C. Hall, M. Fabretto, P. J. Murphy, and D. Evans. Condensation and freezing of droplets on superhydrophobic surfaces. *Advances in Colloid and Interface Science*, 210:47–57, 2014.
- [45] P. Guo, Y. Zheng, , M. Wen, C. Song, Y. Lin, and L. Jiang. Icephobic/Anti-Icing Properties of Micro/Nanostructured Surfaces. *Advanced Materials*, 24(19):2642–2648, 2012.
- [46] A. J. Meuler, J. D. Smith, K. K. Varanasi, J. M. Mabry, G. H. McKinley, and R. E. Cohen. Relationships between Water Wettability and Ice Adhesion. *Applied Materials & Interfaces*, 2(11):3100–3110, 2010.
- [47] S. Farhadi, M. Farzaneh, and S.A. Kulinich. Anti-icing performance of superhydrophobic surfaces. *Applied Surface Science*, 257(14):6264–6269, 2011.
- [48] B.L. Cushing, V.L. Kolesnichenko, and C.J. O’Connor. Recent Advances in the Liquid - Phase Syntheses of Inorganic Nanoparticles. *Chem. Rev.*, 1385(104):3893–3946, 2004.
- [49] W. Stöber, A. Fink, and E. Bohn. Controlled growth of monodisperse silica spheres in the micron size range. *Journal of Colloid and Interface Science*, 26(1):62–69, 1968.
- [50] V.M. Masalov, N.S. Sukhinina, E.A. Kudrenko, and G.A. Emelchenko. Mechanism of formation and nanostructure of Stöber silica particles. *Nanotechnology*, 22(27):275718, 2011.
- [51] C. Leite, E. F. De Souza, and F. Galembeck. Core-and-Shell Nature of Stöber Silica Particles. *J. Braz. Chem. Soc.*, 12(4):519–525, 2001.
- [52] C.J. Brinker and G.W. Scherer. *SOL-GEL SCIENCE: The Physics and Chemistry of Sol-Gel Processing*. Academic Press, Inc., 1990.
- [53] W.A. Zisman. Relation of the Equilibrium Contact Angle to Liquid and Solid Constitution. *Contact Angle, Wettability, and Adhesion*, 43(43):1–51, 1964.
- [54] C.J. Brinker and Alan Hurd. Fundamentals of sol-gel dip-coating. *Journal De Physique*, 4(7):1231–1242, 1994.

- [55] L. Ge, G. Ding, H. Wang, J. Yao, P. Cheng, and Y. Wang. Anti-icing property of superhydrophobic octadecyltrichlorosilane film and its ice adhesion strength. *Journal of Nanomaterials*, 2013, 2013.
- [56] S. A. Mahadik, D. B. Mahadik, M. S. Kavale, V. G. Parale, P. B. Wagh, H. C. Barshilia, S. C. Gupta, N. D. Hegde, and A. V. Rao. Thermally stable and transparent superhydrophobic sol-gel coatings by spray method. *Journal of Sol-Gel Science and Technology*, 63(3):580–586, 2012.
- [57] Q. Shang, Y. Zhou, and G. Xiao. A simple method for the fabrication of silica-based superhydrophobic surfaces. *Journal of Coatings Technology and Research*, 11(4):509–515, 2014.
- [58] S.M Attia, J. Wang, G. Wu, J. Shen, and J. Ma. Review on Sol-Gel Derived Coatings: Process, Techniques and Optical Applications. *J. Mater. Sci. Technol.*, 18(3), 2002.
- [59] W. Siefert. Properties of Thin In₂O₃ and SnO₂ Films Prepared by Corona Spray Pyrolysis, and a Discussion of the Spray Pyrolysis Process. *Thin Solid Films*, 121:275–282, 1984.
- [60] D. Perednis and L. J. Gauckler. Thin Film Deposition Using Spray Pyrolysis. *Journal of Electroceramics*, 14:103–111, 2005.
- [61] Spin coating theory. Brewer Science <http://www.brewerscience.com/research/processing-theory/spin-coating-theory#process-theory>. Last accessed June 13th 2016.
- [62] C. J. Lawrence. The mechanics of spin coating of polymer films. *Physics of Fluids*, 31(10):2786–2795, 1988.
- [63] Michael Quirk and Julian Serda. *Semiconductor Manufacturing Technology*. Prentice Hall, 2001.
- [64] K. Choy. Chemical vapour deposition of coatings. *Progress in Materials Science*, 48(2):57–170, 2003.
- [65] Sigma-aldrich. <http://www.sigmaaldrich.com/catalog/substance/tetraethylorthosilicate208337810411>. Last accessed 21. November 2015.
- [66] Sigma-aldrich. <http://www.sigmaaldrich.com/catalog/product/aldrich/667420>. Last accessed 21. November 2015.

- [67] J. Schindelin, I. Arganda-Carreras, E. Frise, V. Kaynig, M. Longair, T. Pietzsch, S. Preibisch, C. Rueden, S. Saalfeld, B. Schmid, et al. Fiji: an open-source platform for biological-image analysis. *Nature methods*, 9(7):676–682, 2012.
- [68] C. A. Schneider, W. S. Rasband, and K. W. Eliceiri. NIH Image to ImageJ: 25 years of image analysis. *Nature Methods*, 9(7):671–675, 2012.
- [69] J. Goldstein, D. E. Newbury, D. C. Joy, C. E. Lyman, P. Echlin, E. Lifshin, L. Sawyer, and J. R. Michael. *Scanning Electron Microscopy and X-ray Microanalysis*. Springer US, third edition, 2003.
- [70] G. Heydari, M. S. Moghaddam, M. Tuominen, M. Fielden, J. Haapanen, J. M. Mäkelä, and P. M. Claesson. Wetting hysteresis induced by temperature changes: Supercooled water on hydrophobic surfaces. *Journal of Colloid and Interface Science*, 468:21–33, 2016.
- [71] T. Deng, K. K. Varanasi, M. Hsu, N. Bhate, C. Keimel, J. Stein, and M. Blohm. Nonwetting of impinging droplets on textured surfaces. *Applied Physics Letters*, 94(13):13–16, 2009.
- [72] G. Heydari, E. Thormann, M. Ja, E. Tyrode, and P. M. Claesson. Hydrophobic Surfaces : Topography Effects on Wetting by Supercooled Water and Freezing Delay. 2013.
- [73] P. Eberle, M.K. Tiwari, T. Maitra, and D. Poulikakos. Rational nanostructuring of surfaces for extraordinary icephobicity. *Nanoscale*, 6(9):4874–81, 2014.
- [74] Thermal conductivity of some common materials and gases. http://www.engineeringtoolbox.com/thermal-conductivity-d_429.html. Last accessed May 31th 2016.
- [75] J. P. Hindmarsh, A. B. Russell, and X. D. Chen. Experimental and numerical analysis of the temperature transition of a freezing food solution droplet. *Chemical Engineering Science*, 59(12):2503–2515, 2004.

Appendix A

A.1 Synthesis of Nanoparticles

Table A.1: Amount and properties of chemicals in NP synthesis.

Chemical	M_m [g/mol]	ρ [g/mL] at 25 °C	Amount [mL]
Ethanol	0.7895	22.5	
DI water	~ 1	2.5	
NH ₄ OH	0.9	1.5	
TEOS	0.934	0.75	

A.2 Synthesis of β -silane

Table A.2 includes properties of the chemicals used for creating the β -silane sols. These properties were used for calculating volume ratios needed for sol preparation. For the β -40S-sol 6.085 mL ethanol, 0.140 mL DI water pH adjusted by NH₄OH to pH and 1.000 mL of β -silane was used. For the β -5S-sol the ethanol amount was decreased to 0.76 mL, while the amounts of the other chemicals remained unchanged.

Table A.2: Properties of chemicals used in sol synthesis.

Chemical formula	M_m [g/mol]	ρ [g/mL] at 25 °C
$C_{14}H_{19}F_{13}O_3Si$	510.36	1.3299
CH_3OH	46.07	0.7895
NH_4OH	35.05	0.9
H_2O	18.02	1.0

A.3 Surface vs Chamber Temperature

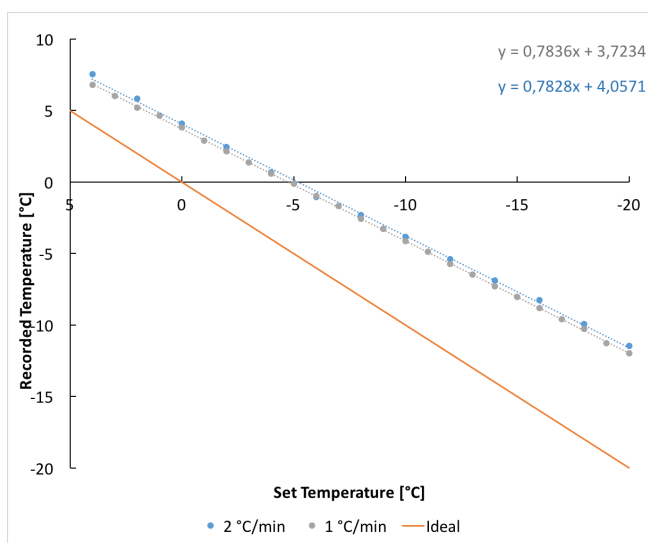


Figure A.1: Recorded temperature as a function of the set temperature during cooling.